Computational analysis of haemodynamic and electrical brain tissue changes during seizures

Peter Hebden

25 January 2019

Contents

1 Introduction

Near Infrared Spectroscopy (NIRS) allows noninvasive monitoring of tissue oxygenation and cerebral haemodynamics. It is particularly well suited to young developmental populations from birth to toddler years [17]. NIRS can be used to measure *in vivo* changes oxygenated haemoglobin (Δ[HbO_2]), deoxygenated haemoglobin (Δ[HHb]), and oxidised cytochrome-c-oxidase (Δ[oxCCO]), an enzyme in the mitochondria associated with tissue metabolism [2].

NIRS has good spatial and temporal resolution, and EEG has excellent temporal resolution. They can be used simultaneously because these modalities have no influence on each other. Consequently, combined measurements may provide additional information about electrical activity as well as local haemodynamics. This multimodal approach has the potential to improve clinical neuromonitoring of preterm and term infants [41].

As part of a collaboration between UCL Medical Physics and Great Ormand Street Hospital, London, *in vivo* brain tissue changes in oxygenation, metabolism, and electrical activity data was collected from Patient 04, a 2.5 year old patient having an epileptic episode.

The aims of this report are to explore the data, apply computational methods to EEG and NIRS measurements in the time and frequency domains to investigate neurovascular and neurometabolic coupling during seizures, and provide a basis for hypothesis generation. It is hoped that by identifying and quantifying how responses

change over time and their interrelationships, it will be possible to increase our understanding of the mechanisms that drive seizure activity. Then NIRS data could be used more reliably for seizure prediction, detection, monitoring conditions during and after seizure events, and provide more information about patient health.

2 Background

2.1 Electroencephalography (EEG)

Epileptogenesis causes functional, structural, or network reorganization changes in the brain that may lead to recurring epileptic seizures [22]. Each seizure results from the abnormal electrical discharge of brain cells. They are associated with high-amplitude EEG spikes, and individual spikes often punctuate the scalp EEGs between attacks [7], but Diagnosis is difficult due to their diversity and complexity. Some take the form of convulsions, while others involve subtle changes in mood, thought, or behaviour. Furthermore, there are many possible causes, including viruses, neurotoxins, tumours, head trauma, and genes [5]. Some cases have been linked to faulty inhibitory synapses (GABAergic) that cause many localized neurons to fire in synchronous bursts [10]; such bursts are rare in normal brains [13].

Diagnosis has traditionally relied heavily on EEG data. In fact EEG revolutionized the entire field of epileptology, and it remains essential to the diagnosis and study of epilepsy and seizures because of its temporal resolution, ease of application and the nature of epileptic conditions themselves [30, Chapter 13]. It is the gold standard in the diagnosis of epilepsy. It measures the electrical activity generated by a large population of hyper-synchronised neurons, mainly localized near the surface of the cortex [42], but small-scale and asynchronous activity is difficult or impossible to measure [8].

2.2 Near Infrared Spectroscopy (NIRS)

2.2.1 NIRS can detect changes in [HbO_2], [HHb], and [oxCCO]

Work on functional NIRS (fNIRS) using HbO_2 and HHb as indicators of the haemodynamic response to neuronal activity has been very substantial since first presented in 1993 due to its many advantages. NIRS is silent, less costly and less susceptible to movement artifacts than other methods [17, 33]. fNIRS is the only noninvasive, *in vivo* method that can assess oxygen consumption during functional tasks [2], and it can measure the CCO signal, which is more brain specific than the haemodynamic signals and, therefore, can indicate cerebral metabolism during neurovascular coupling more directly [23].

For example, the CCO signal response to reduced oxygen delivery in the healthy human brain was examined in [39]. Arterial oxygen saturation was reduced from baseline levels to 80% in eight healthy adult humans. At the nadir of hypoxemia the median changes were as follows: Δ[oxCCO] decreased by 0.24 μM, total haemoglobin concentration increased by 2.83 μM, and the change in haemoglobin difference concentration (Δ[HbD] = Δ[HbO_2] - Δ[HHb]) decreased by 12.72 μM [39].

2.2.2 Broadband NIRS uses more wavelengths to extract more information

An increase in neuronal spiking leads to an increase in cerebral blood flow due to neurovascular coupling, and measurable changes in the local [HbO_2] and [HHb] [44]. NIRS calculates changes in concentration from the changes in the light attenuation in tissue. The proportions of light absorbed, scattered, and transmitted depend on the properties of the medium and the light. Absorbance can be described by the modified Beer–Lambert law

$$A = -\log\left(\frac{I}{I_0}\right) = (c \times \varepsilon_\lambda \times l \times \mathrm{DPF}) + G \tag{1}$$

where A is absorbance, I is intensity of transmitted light, I_0 is intensity of incident light, c is concentration of medium, ε_λ is the molar extinction coefficient characteristic of the medium for light with wavelength λ, and l is distance the light travels in the medium, DPF is the differential pathlength factor and G is the scatter. Scatter is constant and cancels out when changes in chromophore concentrations are calculated over two time points [17].

Calculating and validating changes in haemoglobin (Hb) is easy because its concentration in tissue is high, but the signal from CCO is about 5% to 10% as large as haemoglobin's. So light attenuation changes due to CCO can easily be masked by the much larger attenuation changes due to HbO_2 and HHb, i.e. cross-talk [2].

Using more wavelengths tends to reduce cross-talk and noise. The gold standard for broadband NIRS systems requires 780 to 900 at 1 wavelength resolution. However, the aim is to resolve the shape of the oxidised-reduced CCO spectra and disentangle it from the other chromophores. Arifler *et al.* [1] found that the optimum eight wavelengths were 784, 800, 818, 835, 851, 868, 881, and 894, as in Figure 1.

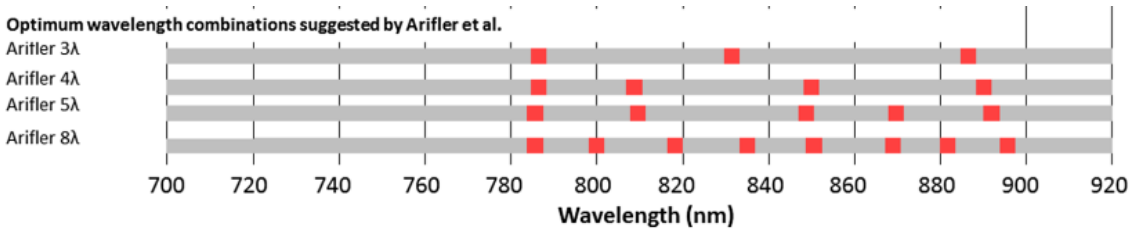

Figure 1: Optimal wavelength combinations. Image: [1].

The algorithm, determination of chromophore absorption spectra, estimation of the optical pathlength, and number and choice of wavelengths should reduce the impact of artifacts [2]. Broadband NIRS and the UCLn algorithm can accurately resolve spectral changes due to oxCCO without cross-talk from the haemoglobin chromophores [26].

Using Equation 2, changes in chromophore concentrations were calculated from measured changes in broadband NIR light attenuation using the modified Beer-Lambert law as applied with the UCLn algorithm [4]. This algorithm is a least-squares fitting procedure based on multiple regression analysis designed to determine the best fit of the chromophore extinction coefficients ε to the measured attenuation changes ΔA over n of wavelengths λ:

$$\begin{bmatrix} \Delta[\mathrm{HbO_2}] \\ \Delta[\mathrm{HHb}] \\ \Delta[\mathrm{oxCCO}] \end{bmatrix} = \frac{1}{pathlength} \begin{bmatrix} \varepsilon_{HbO_2}(\lambda_1) & \varepsilon_{HHb}(\lambda_1) & \varepsilon_{oxCCO}(\lambda_1) \\ \varepsilon_{HbO_2}(\lambda_2) & \varepsilon_{HHb}(\lambda_2) & \varepsilon_{oxCCO}(\lambda_2) \\ \vdots & \vdots & \vdots \\ \varepsilon_{HbO_2}(\lambda_n) & \varepsilon_{HHb}(\lambda_n) & \varepsilon_{oxCCO}(\lambda_n) \end{bmatrix} \begin{bmatrix} \Delta A(\lambda_1) \\ \Delta A(\lambda_2) \\ \vdots \\ \Delta A(\lambda_n) \end{bmatrix} \quad (2)$$

The UCLn algorithm was used to solve for changes in the chromophore concentrations across 136 wavelengths [4].

In [4], Bale *et al.* presented a novel lens-based broadband NIRS system, the "CYtochrome Research Instrument and appLication" (CYRIL). This system was developed to simultaneously measure cerebral changes in tissue oxygenation and haemodynamics indirectly by estimation of the changes in [Hb] and utilisation of oxygen via the measurement of the oxidation state of CCO. A lens-based system was chosen because they have a higher throughput of light than mirror-based spectrographs. This system used a grating that provided a wavelength resolution of 0.27nm ±0.70nm and 136nm bandwidth. It was mounted on a platform and rotated to set the range of wavelengths to resolve. The 770nm–906nm range was chosen [4]; oxCCO is a strong absorber at 830nm [40]. After diffraction at the grating, the light was focused onto the charge coupled device (CCD detector) with an f/2 focusing lens. Focusing the light in the y-direction reduces cross-talk between the detector channels[4].

In [2], Bale *et al.* presented a new multichannel broadband NIRS (bNIRS) system. It can measure changes in light attenuation of 308 NIR wavelengths (610nm to 918nm) and quantify the $\Delta[\mathrm{HbO_2}]$, $\Delta[\mathrm{HHb}]$ and $\Delta[\mathrm{oxCCO}]$ simultaneously over 16 different brain locations.

2.2.3 Broadband NIRS can detect seizures and monitor patients

Near-infrared spectroscopy (NIRS) measurements of CCO have the potential to yield crucial information about cerebral metabolism [2], especially if CCO is a more brain-specific marker of functional activation [11].

Seizures are common following hypoxic-ischemic brain injury in newborn infants, and prolonged or recurrent seizures may exacerbate neuronal damage in the developing brain. CCO is responsible for more than 90% of ATP production inside mitochondria and is a potential biomarker. Using a broadband NIRS system, Mitra *et al.* measured the changes in $\Delta[\mathrm{oxCCO}]$) and haemodynamics during recurrent seizures following hypoxic-ischemic encephalopathy in a newborn infant [28]. They made several observations:

1. A rapid increase in $\Delta[\mathrm{oxCCO}]$ at the onset of seizures together with a rise in the baseline of amplitude-integrated electroencephalogram.

2. Cerebral oxygenation and cerebral blood volume fell shortly before seizure onset, then recovered rapidly during seizures.

3. $\Delta[\mathrm{oxCCO}]$ during seizures correlated with changes in mean EEG voltage, which implies an increase in neuronal activation and energy demand.

4. Progressive decline in the $\Delta[\mathrm{oxCCO}]$ baseline during seizures implies a progressive decrease of mitochondrial oxidative metabolism [28].

Bale et al. demonstrated that a strong relationship between cerebral metabolism (broadband NIRS-measured CCO) and cerebral oxygenation was associated with unfavourable outcome of newborn brain injury. This was probably due to a lower cerebral metabolic rate and mitochondrial dysfunction in severe encephalopathy [3].

3 Methods

The HR can be modeled by a gamma function [6], as in Figure 2. The haemodynamic response is slow [37]. Typical fMRI temporal resolution ∼2 seconds (s), and typical spatial resolution is ∼3mm^3.

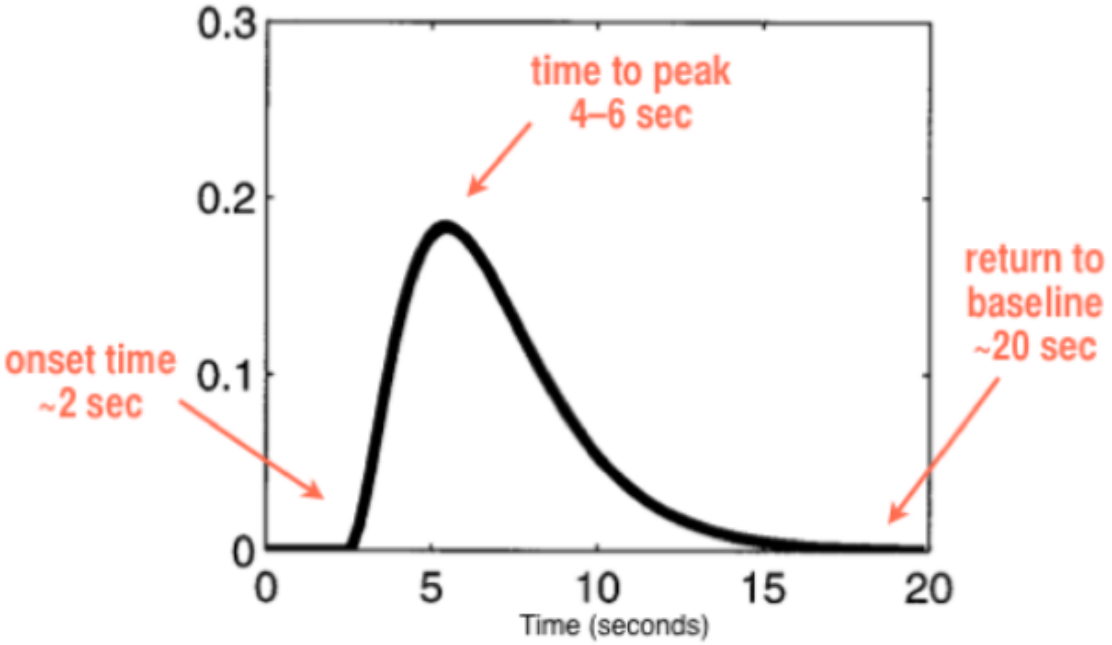

Figure 2: BOLD haemodynamic response function: the gamma function can model the HR. Response timing: ∼2s delay, 4–6s to peak, up to 20s back to baseline. Image: [6].

3.1 Computer Software

I used Matlab R2018b, [`https://uk.mathworks.com`], for all computation and plots. Matlab function names are in this font `name`.

3.2 EEG and NIRS maps

Figure 3 shows the NIRS channel locations. Figure 4 shows the EEG electrode locations; the available locations of interest are circled in green, F4, C4, and F3 and C3. Note: the mapping from electrode number → electrode location name was confirmed by inspecting the Matlab data structure **eeg_details.label** and the EDF header data structure **header.label**.

The following NIRS→EEG pairs of proximate locations were used for data analysis in this report.

- Right side of head: R1→F4, R2→F4, R3→C4, R5→C4.

- Left side of head: L1→F3, L2→F3, L3→C3, L4→C3.

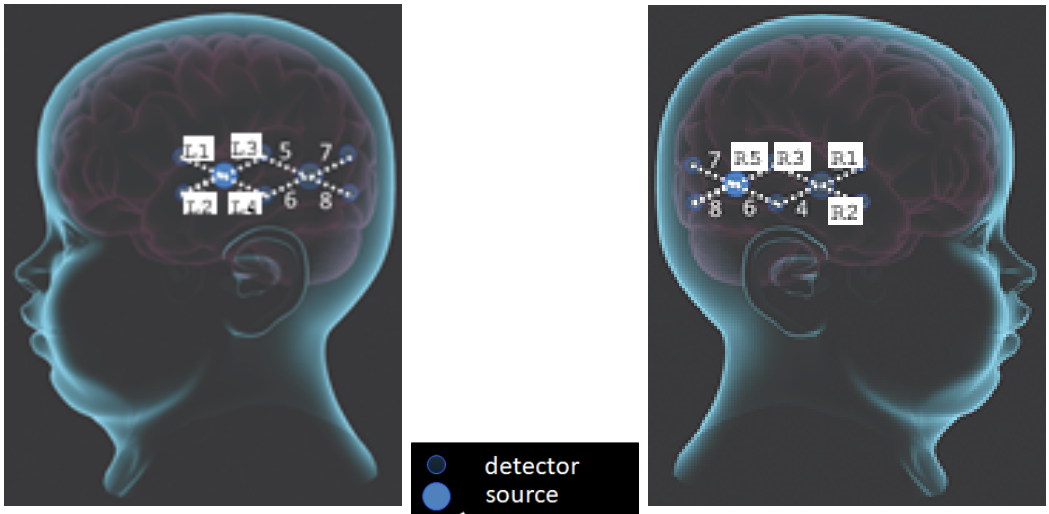

(a) Left: L1, L2, L3, L4

(b)

(c) Right: R1, R2, R3, R5

Figure 3: NIRS data was recorded from eight locations: (a) L1, L2, L3, L4 over the left temporal lobe, and (c) R1, R2, R3, R5 over the right temporal lobe. Images: modified from Isabele de Rover, UCL.

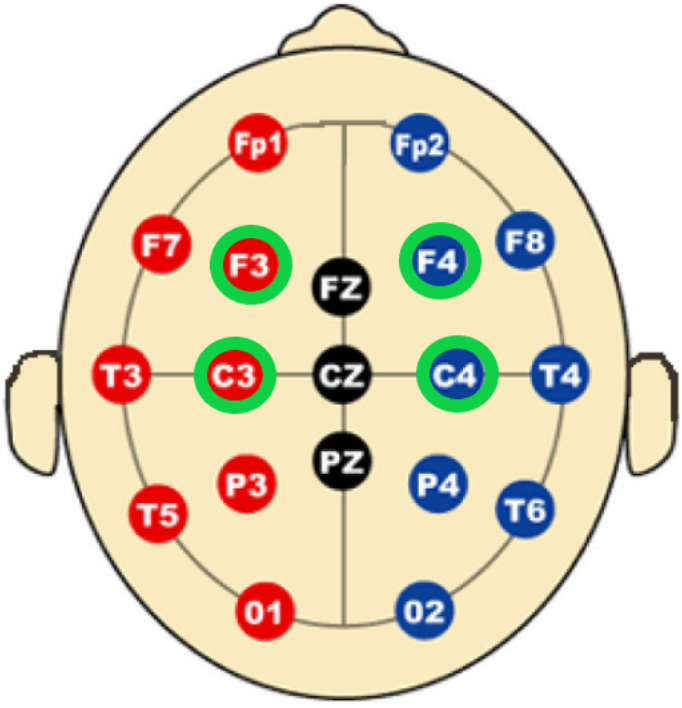

Figure 4: Surface map of EEG electrode locations. The four available locations closest to the eight NIRS channels in this report are circled in green. Image: modified from `https://openi.nlm.nih.gov`.

3.3 EEG data and seizure annotations

From this patient's history, the EEG was difficult to annotate due to constant pathology even between seizures. Nonetheless, the neurophysiology consultant identified

seizure onset and offset times. These times are used for all data analysis.

This data includes 17 generalised seizures. Seizure lengths were much more variable that the time between seizures. Mean seizure length 81.71 seconds (s), standard deviation 36.88s. Mean time between seizures 103.25s, standard deviation 15.81s.

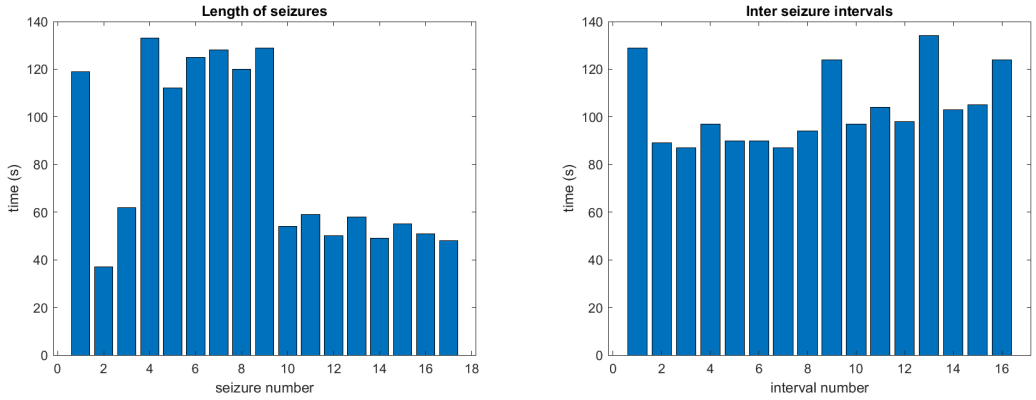

(a) (b)

Figure 5: Seizure statistics: (a) seizure lengths: mean 81.7s, standard deviation 36.88s, (b) time between seizures: mean 103.25s, standard deviation 15.81s.

3.4 Data Filters

3.4.1 EEG filters and artifact removal

The correct use of filters provides one of the major sources of contention among electroencephalographers and technologists [30, p149]

- The EEG data was sampled at 256Hz in units of mV.
- The EEG data might have been filtered by hardware, e.g. a broad bandpass filter.

All filters were constructed from second order Butterworth filters and the `filtfilt` function to zero phase filter the data.

Typical high-pass filter cut-offs are in the 0.5 to 1Hz range. They filter out slow artifacts, such as electrogalvanic signals and movements [30]. Typical low pass filter cut-offs are in the 35 to 70Hz range. They filter out high-frequency artifacts, such as electromyographic signals [30].

I applied two filters in a cascade: low pass with a 35Hz cut-off, then a high pass with a 0.5Hz cut-off. The low pass filter was applied first to promote filter stability.

The remaining 50Hz artifact was removed by a stopband filter with cut-off frequencies 50Hz $\pm$ 0.3

Next remaining large artifacts were identified according to two thresholds. A high threshold was used for detection; a low threshold was used for extension. Each artifact detected by the high threshold was extended to neighboring points greater than the low threshold ($\sim$66% of the high threshold).

The artifact data points were set to *not a number* (NaN) to mark those values as missing, then missing values were interpolated with `interp1` function using the default linear method.

The high threshold T for each EEG trace was defined as a multiple of each trace's median absolute deviation, which is robust to extreme values [34]. T was calculated using Equation 3

$$T = M \times \sigma; \qquad \sigma = \frac{\text{median}|X|}{0.6745} \tag{3}$$

where $M = 15$ is the multiplier, σ is the median absolute deviation, $|X|$ is the absolute value of the filtered data, and the denominator 0.6745 is derived from the inverse of the cumulative distribution function for the standard normal distribution evaluated at 0.75 [35]. In other words, the area under the curve left of 0.6745 standard deviations equals 0.75.

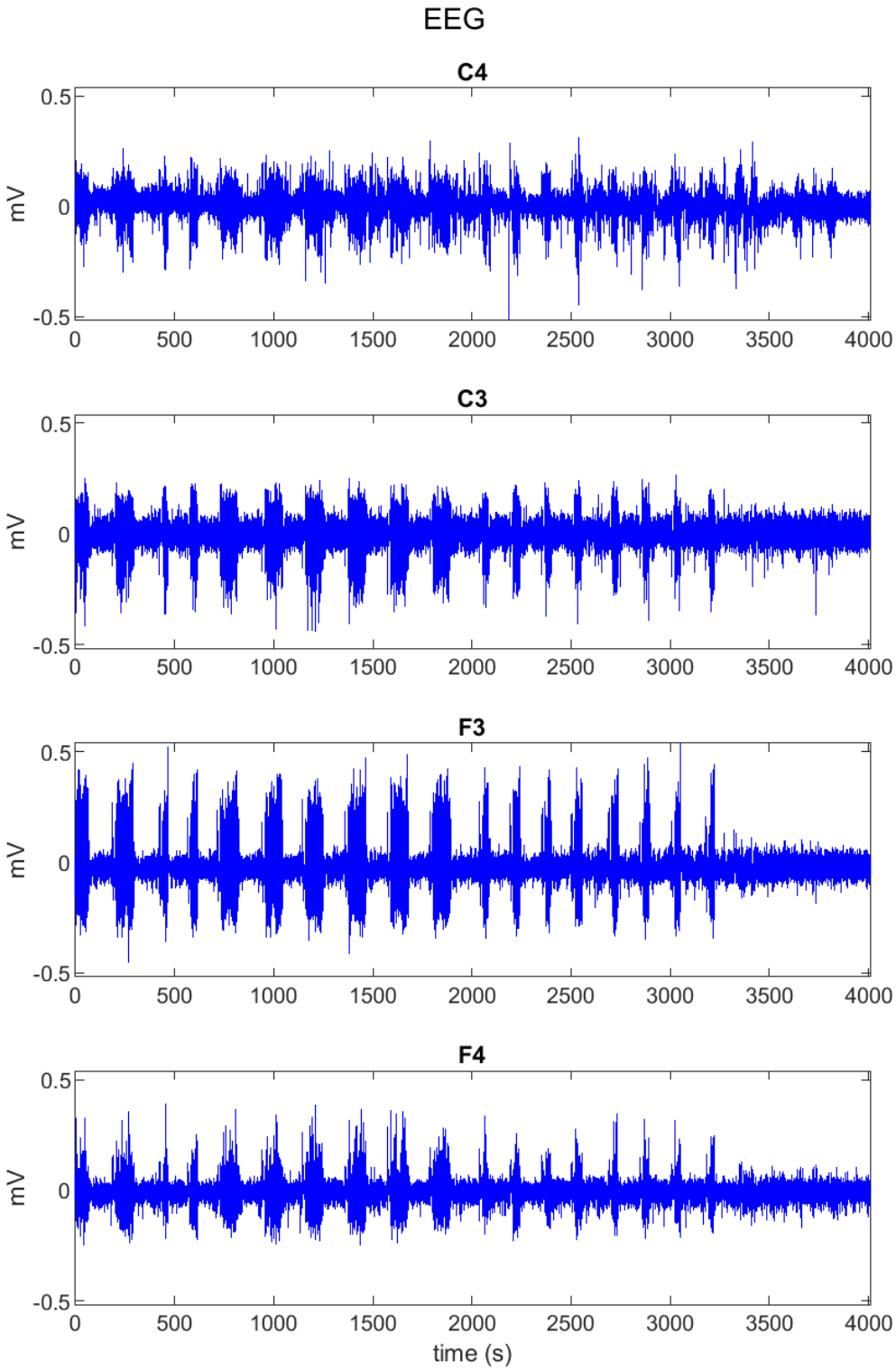

Figure 6: EEG not filtered by software.

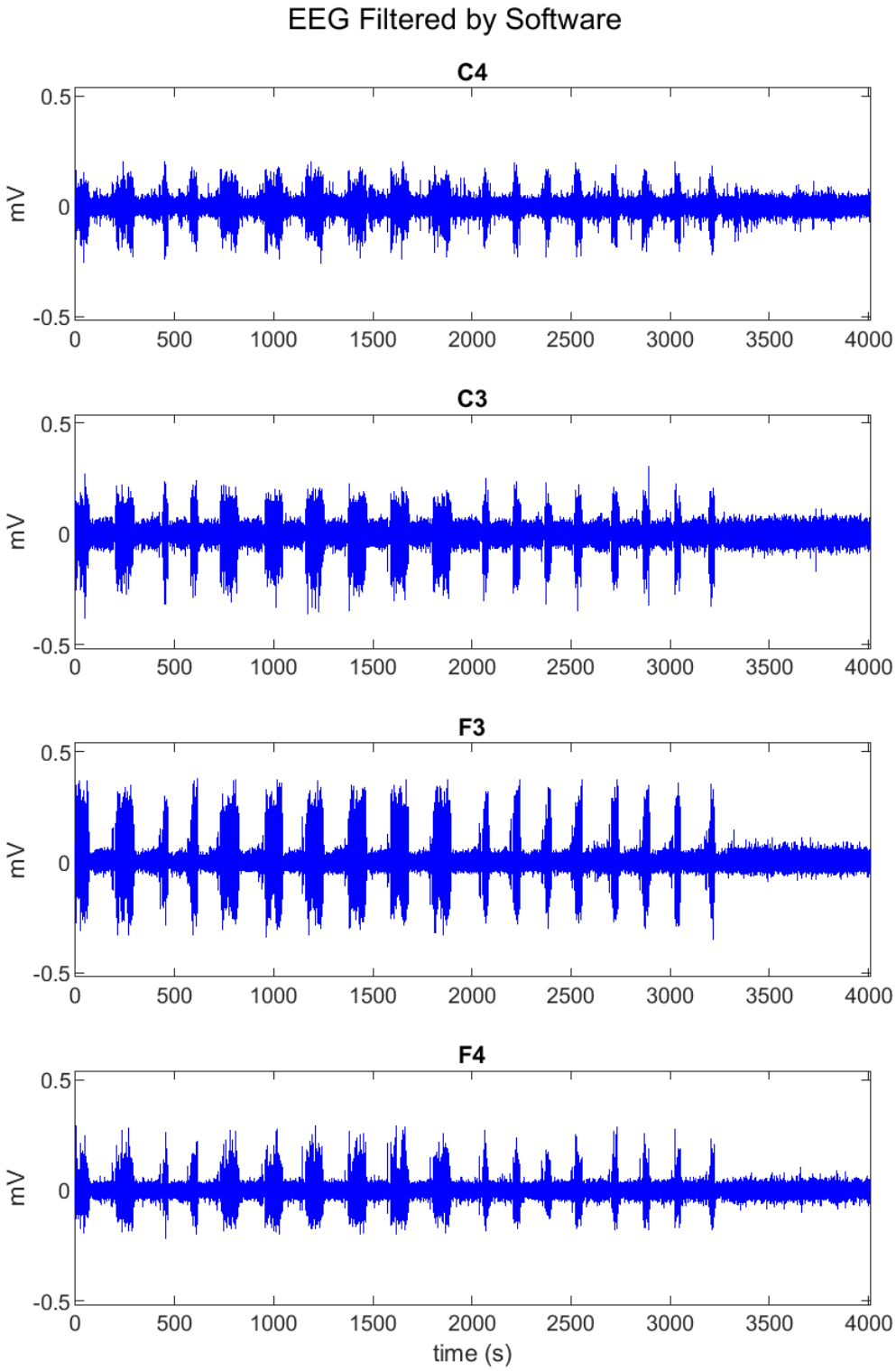

Figure 7: EEG filtered and artifacts removed.

3.4.2 NIRS filters

A common practice in fNIRI signal processing is to band-pass or low-pass filter the signals to remove non-evoked components using a 0.2Hz cut-off frequency [36]. To remove low frequency drift and cardiac oscillations data can be band-pass filtered with, for example, a third order Butterworth filter between 0.01 and 0.5Hz [9] (original sampling rate was 25Hz). The NIRS data described in [15] was bandpass filtered between 0.02–0.5Hz.

The NIRS data was sampled at 0.5Hz, interpolated to 1Hz. The unfiltered data in Figures 8, 10, and 12 show a slow drift, especially for some channels. I used a high pass filter with a 0.02Hz cut-off, but a $\sim$0.005Hz cut-off might be preferred to preserve more of the very low frequency changes. Filtered data is in Figures 9, 11, and 13.

Nonetheless, filtering had little impact on the NIRS results. For example, 17 spikes that correspond to 17 seizures recorded at NIRS channel R3 are obvious in both Figures 8 and 9.

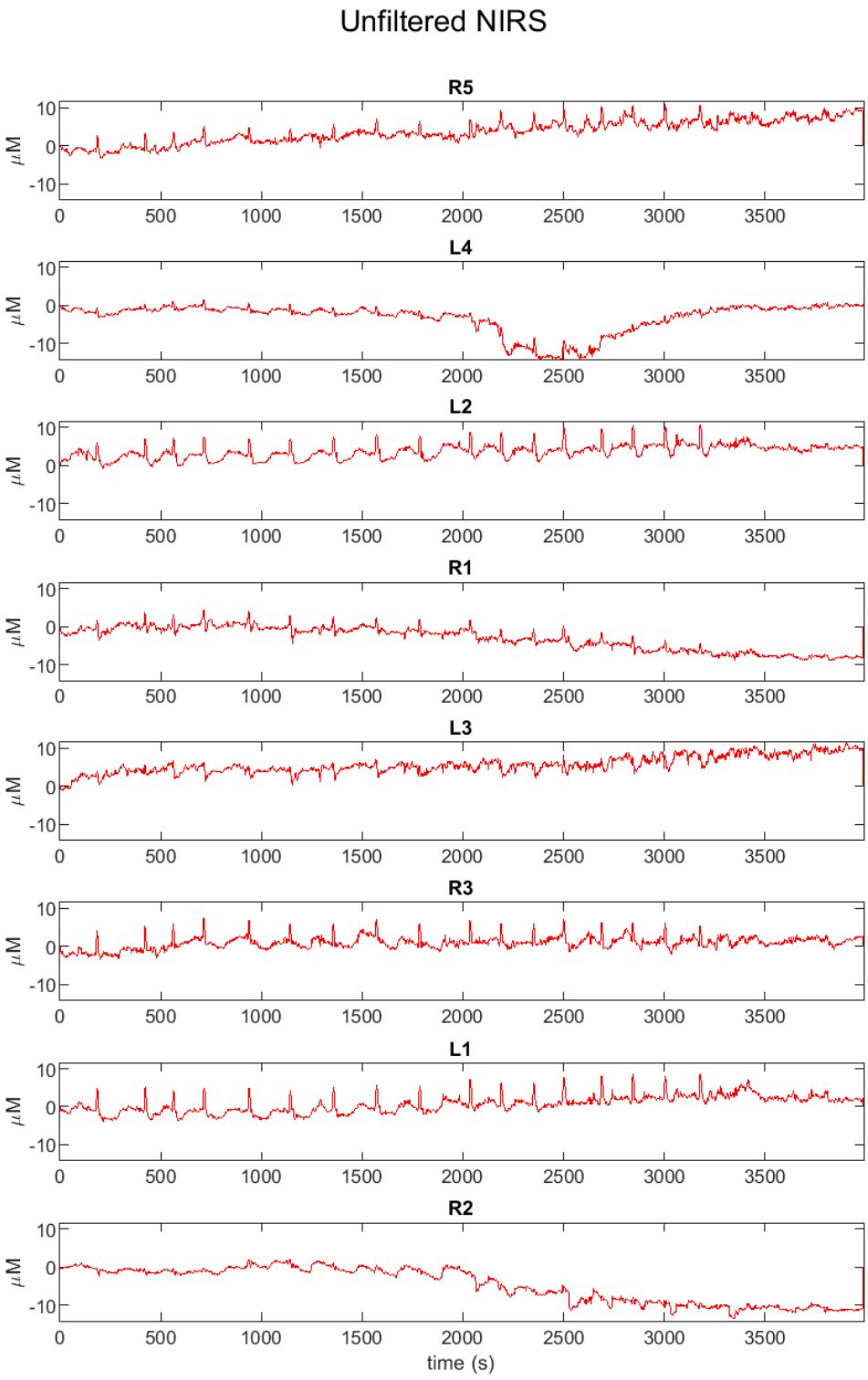

Figure 8: Unfiltered NIRS $\Delta[HbO_2]$ per location.

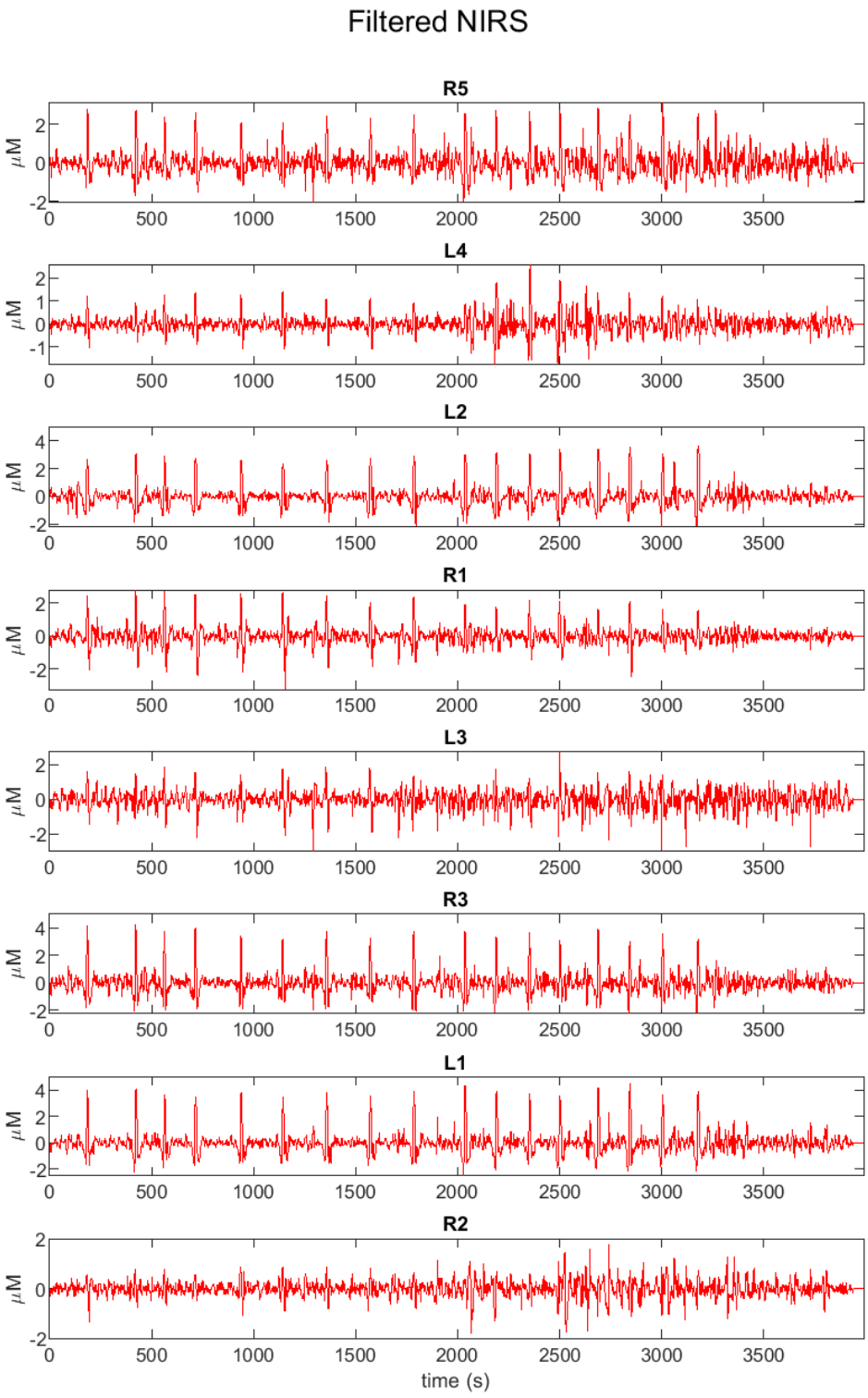

Figure 9: Filtered NIRS $\Delta[HbO_2]$ per location. Note the different scales.

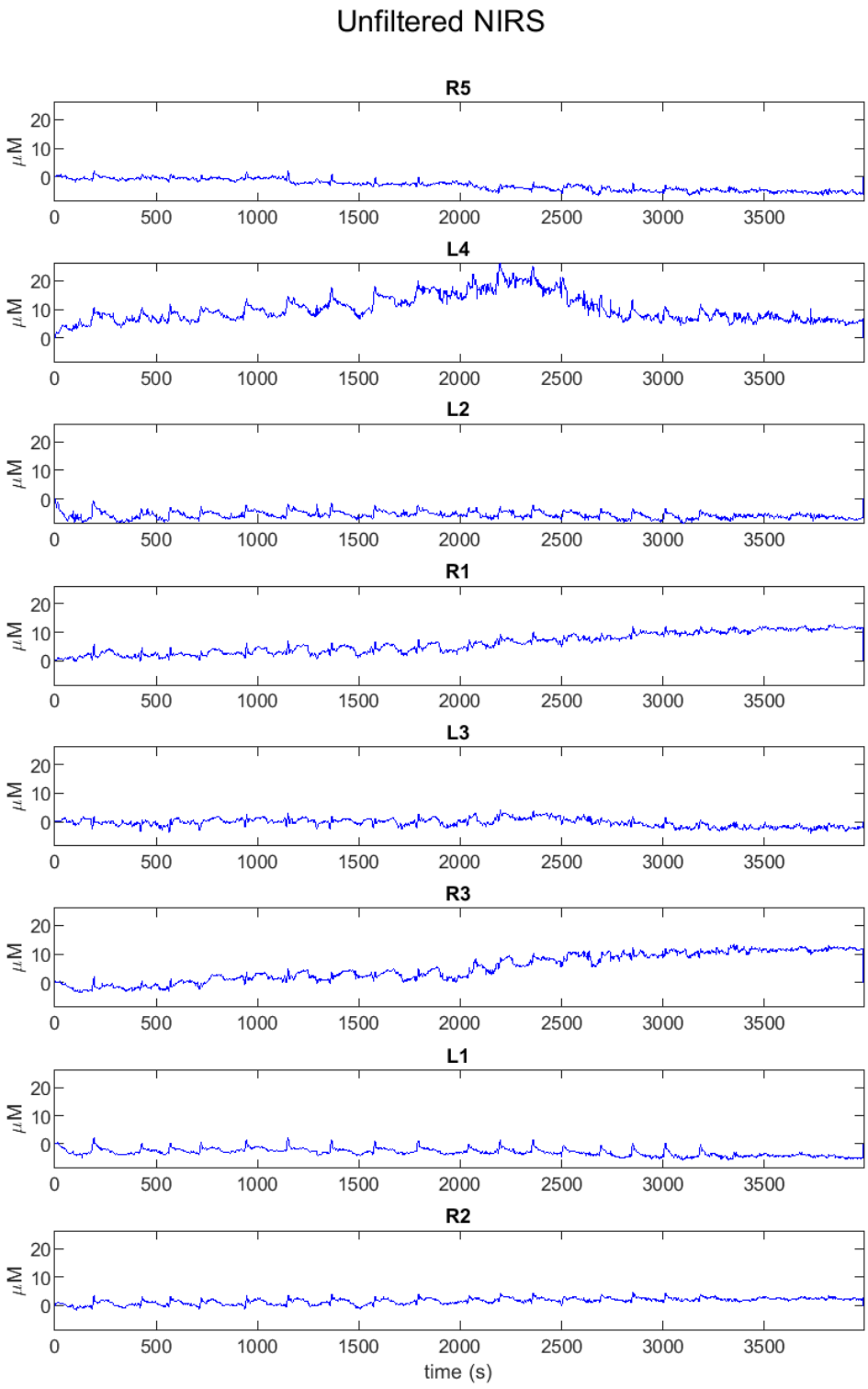

Figure 10: Unfiltered NIRS Δ[HHb] per location.

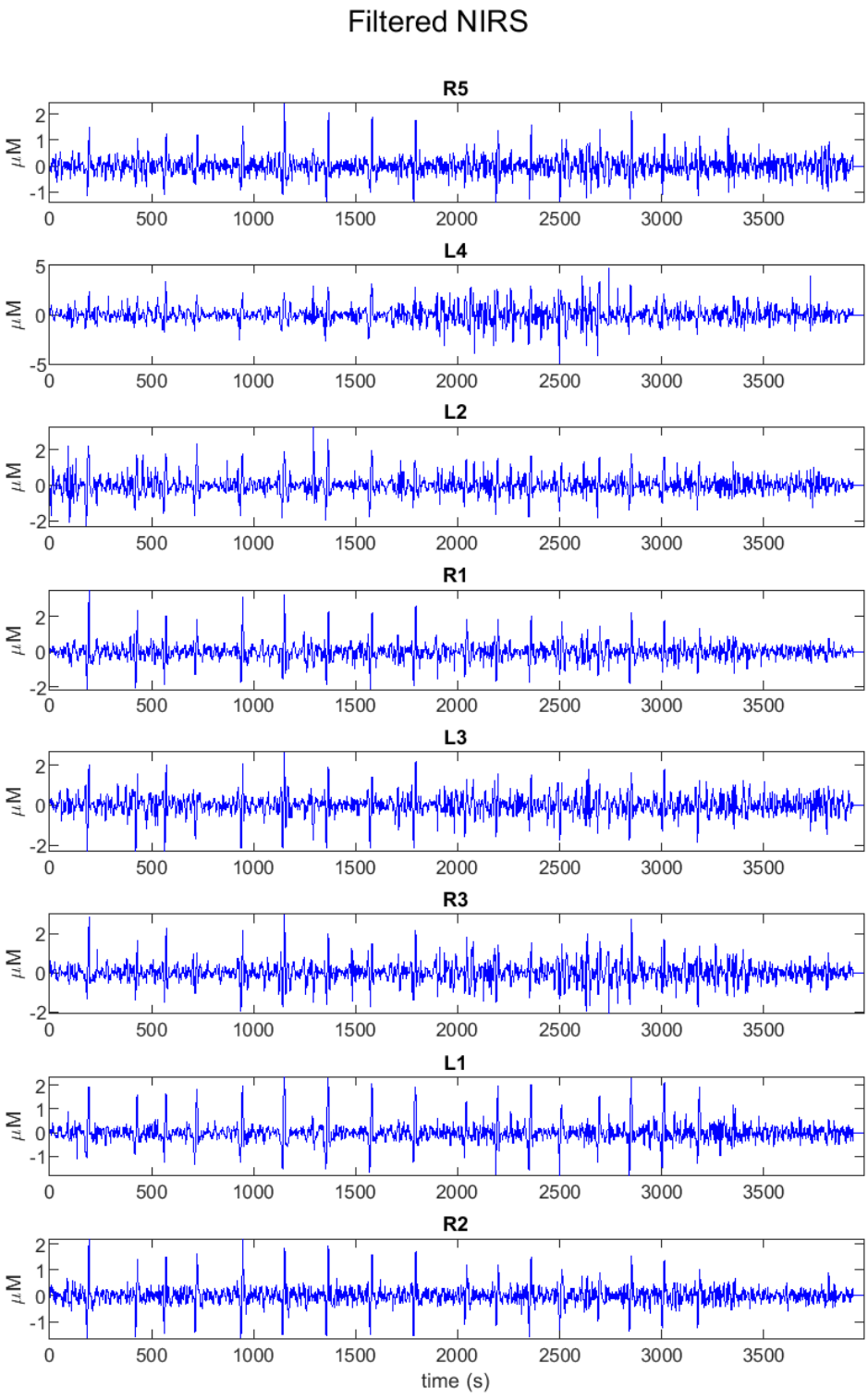

Figure 11: Filtered NIRS Δ[HHb] per location. Note the different scales.

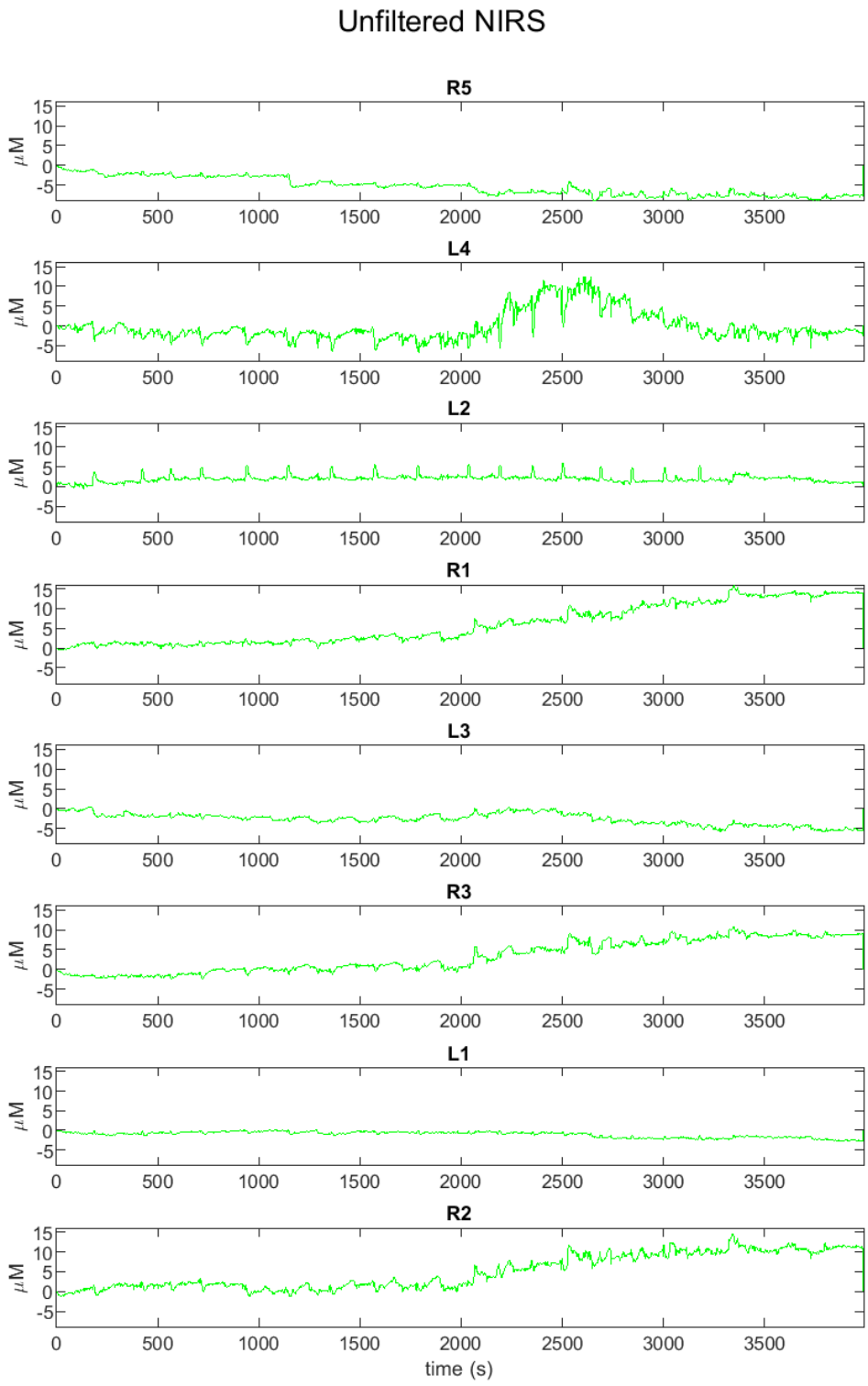

Figure 12: Unfiltered NIRS Δ[oxCCO] per location.

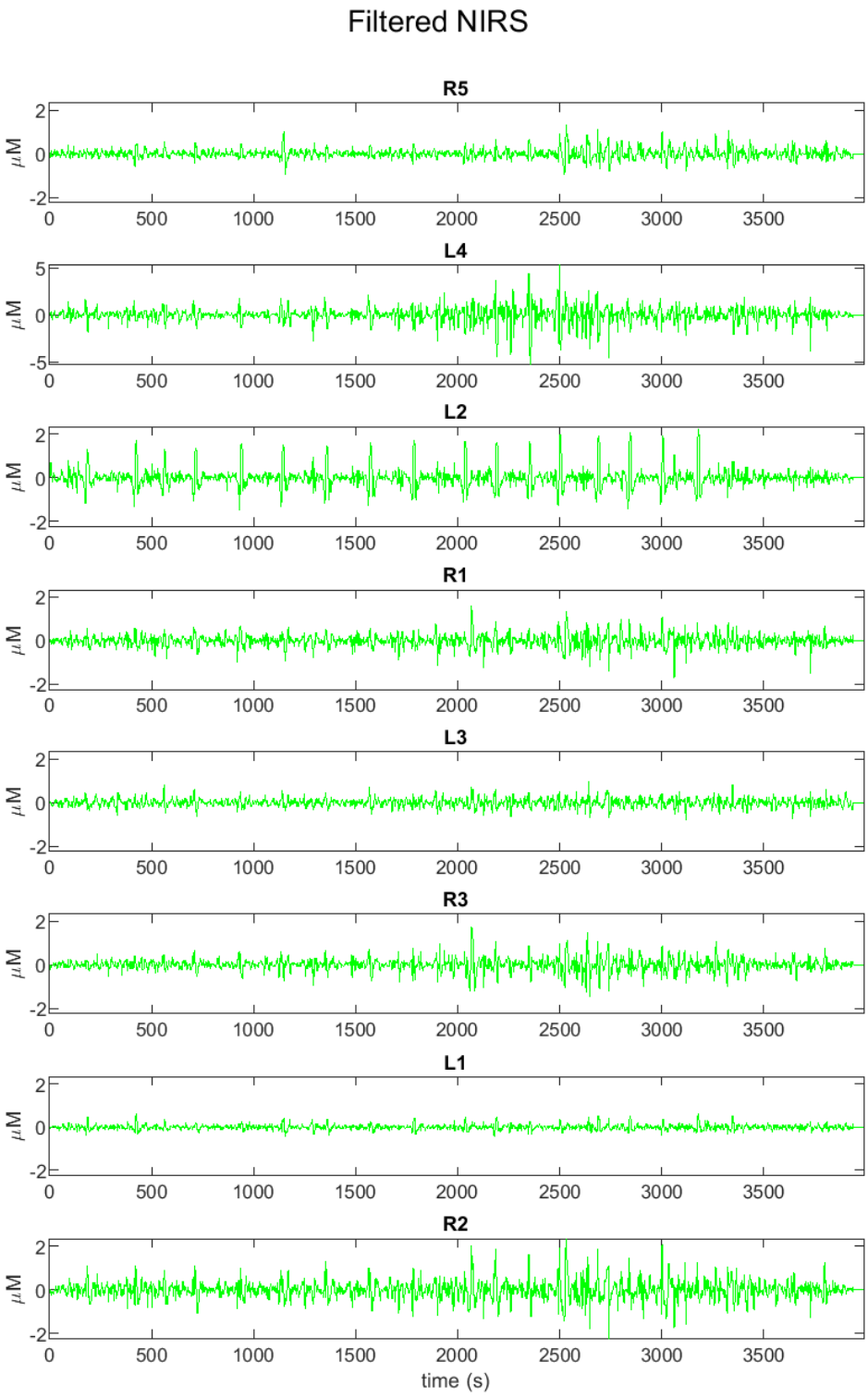

Figure 13: Filtered NIRS Δ[oxCCO] per location. Note the different scales.

3.5 NIRS waveform extraction

All waveform extractions were based on 17 seizure detection times. They were averaged to produce a mean waveform of the same length for each channel, Some waveforms were peak aligned first to produce a mean waveform for each channel with a higher and sharper peak.

The seizure/peak aligned waveforms are in Section 4.6.1. The algorithm for peak alignment was as follows. For each channel and for each seizure, each of the five waveforms were peak aligned relative to the after detection time window. The waveforms that peaked before the mid point of the time window (40s after detection, inclusive) were shifted left by negative seconds, waveforms that peaked after the mid point were shifted right by positive seconds. The mean and standard deviation of the shifts, in seconds (rounded), for each waveform are in Table 1.

3.6 FFT and spectrograms

FFTs were generated with `fft`, and spectrograms were generated with `spectrogram` using parameters `[128,120,128, 256, 'yaxis']`. Yellow colours indicate frequency content with relatively high power.

3.7 Decimation

EEG data was decimated from 256Hz down to 1Hz with the `decimate` function using the default eighth-order lowpass Chebyshev Type I filter. However, decimate also greatly reduces the amplitude of the data. Figure 14 shows a side by side comparison.

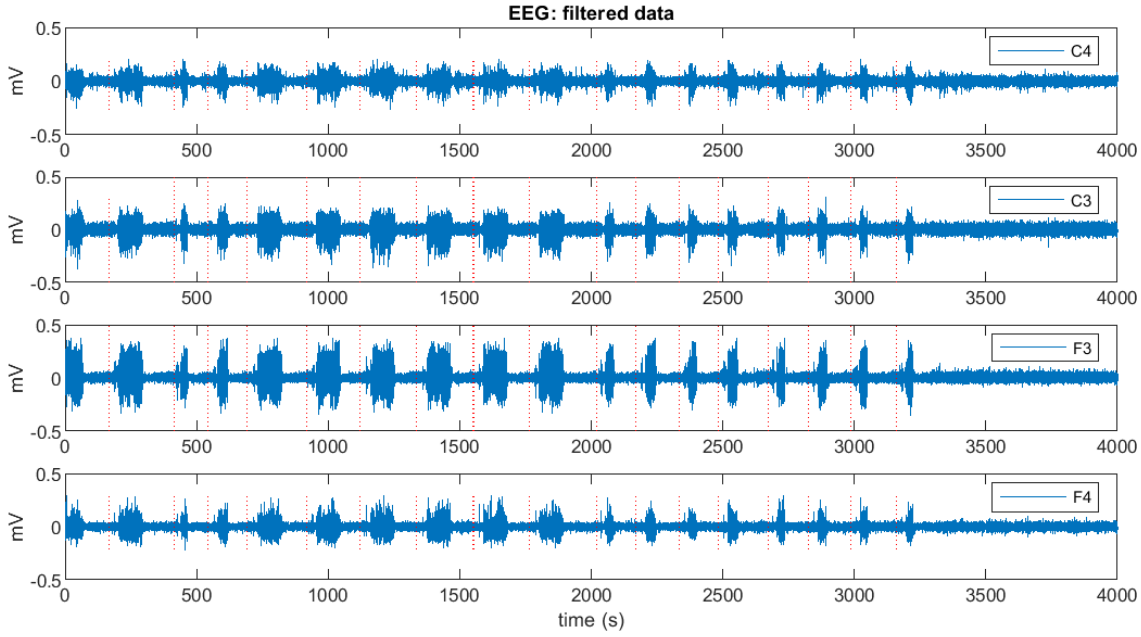

(a)

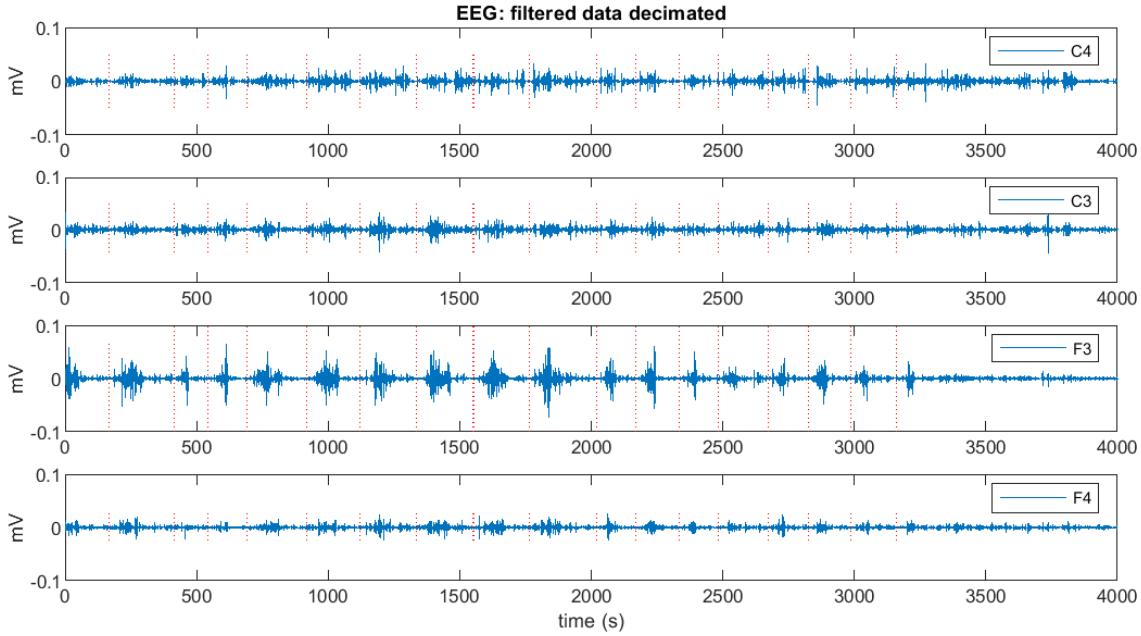

(b)

Figure 14: EEG data (a) filtered, (b) filtered and decimated. Note the different scales.

3.8 Correlation

Pearson correlation coefficients (ρ) were computed with `corrcoef`, it uses the equation

$$\rho(A,B) = \frac{1}{N-1}\sum_{i=1}^{N}\left(\frac{A_i-\mu_A}{\sigma_A}\right)\left(\frac{B_i-\mu_B}{\sigma_B}\right). \tag{4}$$

where μ and σ are the mean and standard deviation of their respective variables, and ρ is a measure of the linear dependence of the two variables A and B.

In Section 4.5, unfiltered and filtered EEG was correlated with filtered NIRS $\Delta[\mathrm{HbO}_2]$ by correlating the area under the smoothed absolute EEG curve per sec-

ond with NIRS $\Delta[HbO_2]$ per second:

$$\text{eeg} = \texttt{smooth}(\texttt{abs}(\texttt{decimate}(\texttt{eeg\_data}, 256)), 30) \tag{5}$$
$$\text{nirs} = \texttt{smooth}(\texttt{nirs\_data}, 30) \tag{6}$$
$$\rho = \texttt{corrcoef}(\texttt{trapz}(\texttt{eeg}), \texttt{nirs}), \tag{7}$$
$$\tag{8}$$

where the EEG window was phase shifted by 21s or 36s $\pm$ {1,2} seconds of jitter, and the NIRS window was phased shifted by 16s (after detection). Data window was 13s.

In Sections 4.6.3, 4.6.4, and 4.6.5, EEG data was decimated down to 1Hz, then the absolute value (`abs`) of this data was correlated with NIRS data. Data window was 40s.

For all figures each correlation ρ was performed relative to a seizure detection time and set to zero when not statistically significant, i.e. p-value was ≥ 0.05.

3.9 Principal component analysis

The aim of principal component analysis (PCA) is to represent the d-dimensional data in a lower-dimensional space that best expresses the variation in a sum-squared error sense. For example, PCA might reduce 40 features to 3 principal components that account for over 80% of data variance. Ideally, a domain expert can suggest the number of components ahead of time, as is the case with clustering [38].

PCA was applied to the NIRS data. In general, given data recorded from the 8 locations of interest, 136 data segments relative to the 17 seizure detection times was stored in a 2D matrix M with 136 rows.

Algorithm 1 shows the code used for PCA and clustering. Set the percent of variance, construct the covariance matrix with `cov`, do eigenvalue decomposition with `eig`, sort eigenvalues, find minimum number of dimensions N that account for a user defined percent of variance (80% in this case), extract the minimum number of eigenvectors, and project the data M (waveforms, for example) onto a lower dimensional space using matrix multiplication.

After PCA the N principal components (PC) of each waveform were clustered by `kmeans` into k clusters using the distance metric *squared euclidean distance*; the best set of clusters out of 20 replicates were returned by the `kmeans` function where each replicate used different initial random centroids. The returned cluster numbers are in the same order at the corresponding waveforms.

Data: time series
Result: dimension reduction and clustering of waveforms
pct=0.80;
C = cov(M);
[V,D] = eig(C);
[eigen_values, eigen_value_indices] = sort(diag(D), 'descend') ;
N = find((cumsum(eigen_values)/sum(eigen_values)) > pct,1);
V_low = V(:,eigen_value_indices(1:N)) ;
PC = M * V_low;
cluster_numbers = kmeans(PC, k, 'Distance','sqeuclidean','Replicates',20);

Algorithm 1: Code for principal component analysis and k-means.

3.10 K-means clustering

K-means [25] is an algorithm for finding structure in multidimensional data sets [24]; it is a form of unsupervised learning [21]. Although simple and proposed over 50 years ago, it is still popular and widely used [20]. Essentially, k-means clusters similar objects together based on a distance metric, e.g. Euclidean distance. This is the straight line distance between the features of each waveform and the features of the nearest centroid.

In this paper, clustering starts with a matrix of 136 waveforms recorded from all locations, either EEG electrodes or NIRS channels. The waveforms were extracted from time series data relative to the seizure detection time. They vary in shape and amplitude. The k-means clustering algorithm grouped waveforms with similar features (principal components) together based on the Euclidean distance metric. Since the true number of clusters is not known, the number of clusters must be estimated.

In general, compact and well separated clusters score high for quality [20]. `kmeans` and `eva` functions use various metrics to estimate the optimal number of clusters, but the final choice of k still depends on domain expertise. The number of clusters k was set to 8, 4, and 2 to show the 136 clustered waveforms at various level of granularity and evaluation but, based on domain expertise and space limitations, figures showing k=8 and k=4 have been omitted from this report.

4 Results

4.1 FFTs of EEG traces from each electrode

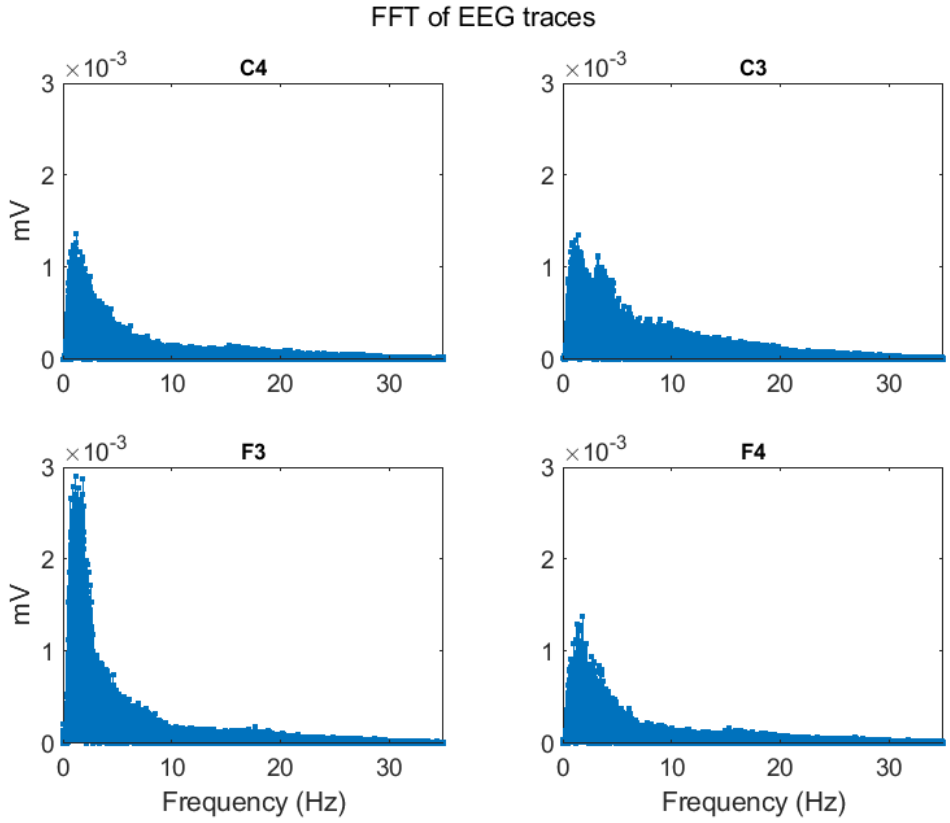

Figure 15: FFT of filtered EEG traces.

4.2 Spectrograms of EEG traces from each electrode

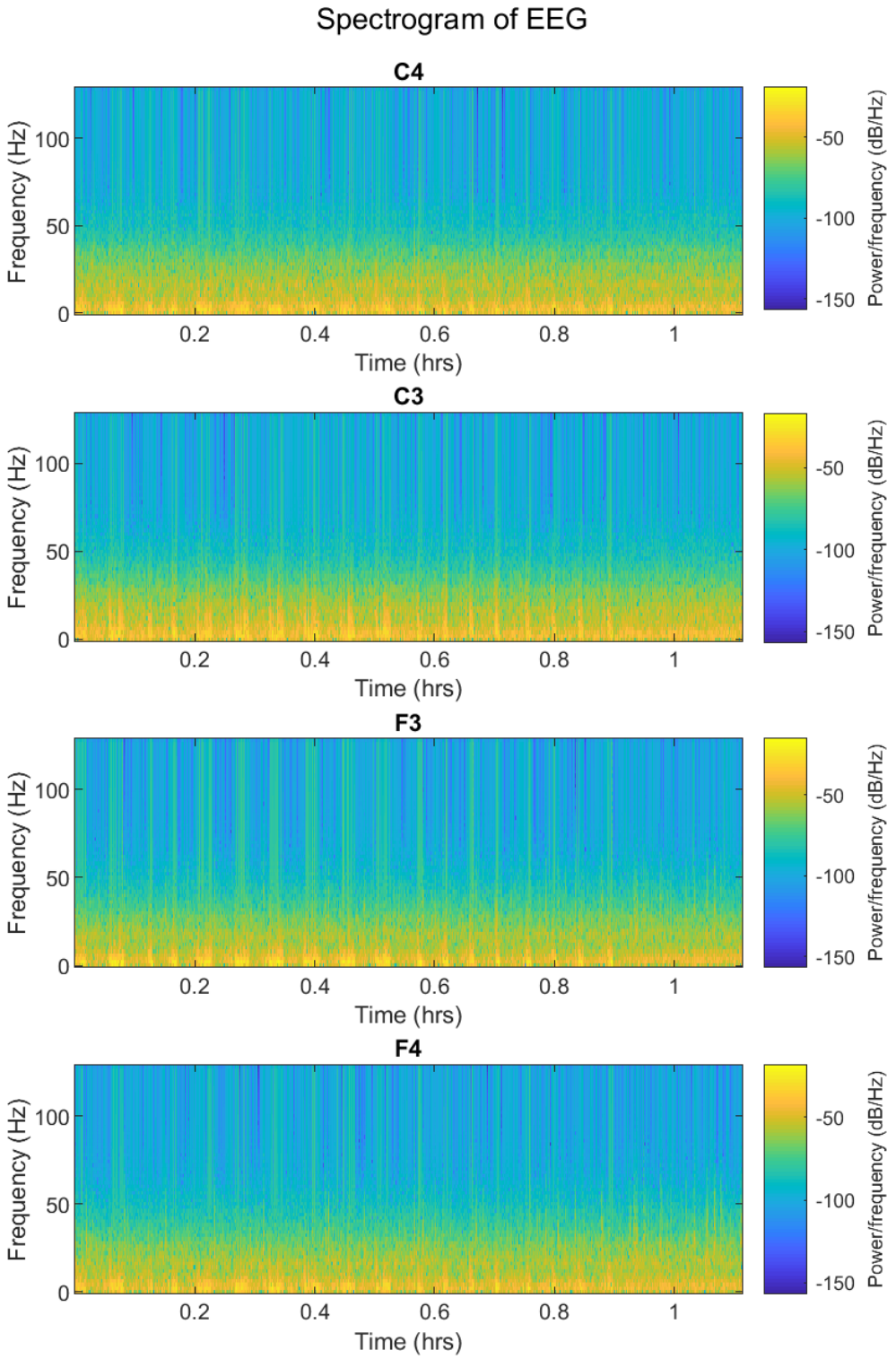

Figure 16: Spectrograms of EEG traces. Seizures are indicated by the bright yellow patches along the horizontal axis.

4.3 FFTs of NIRS $\Delta[HbO_2]$ from each channel

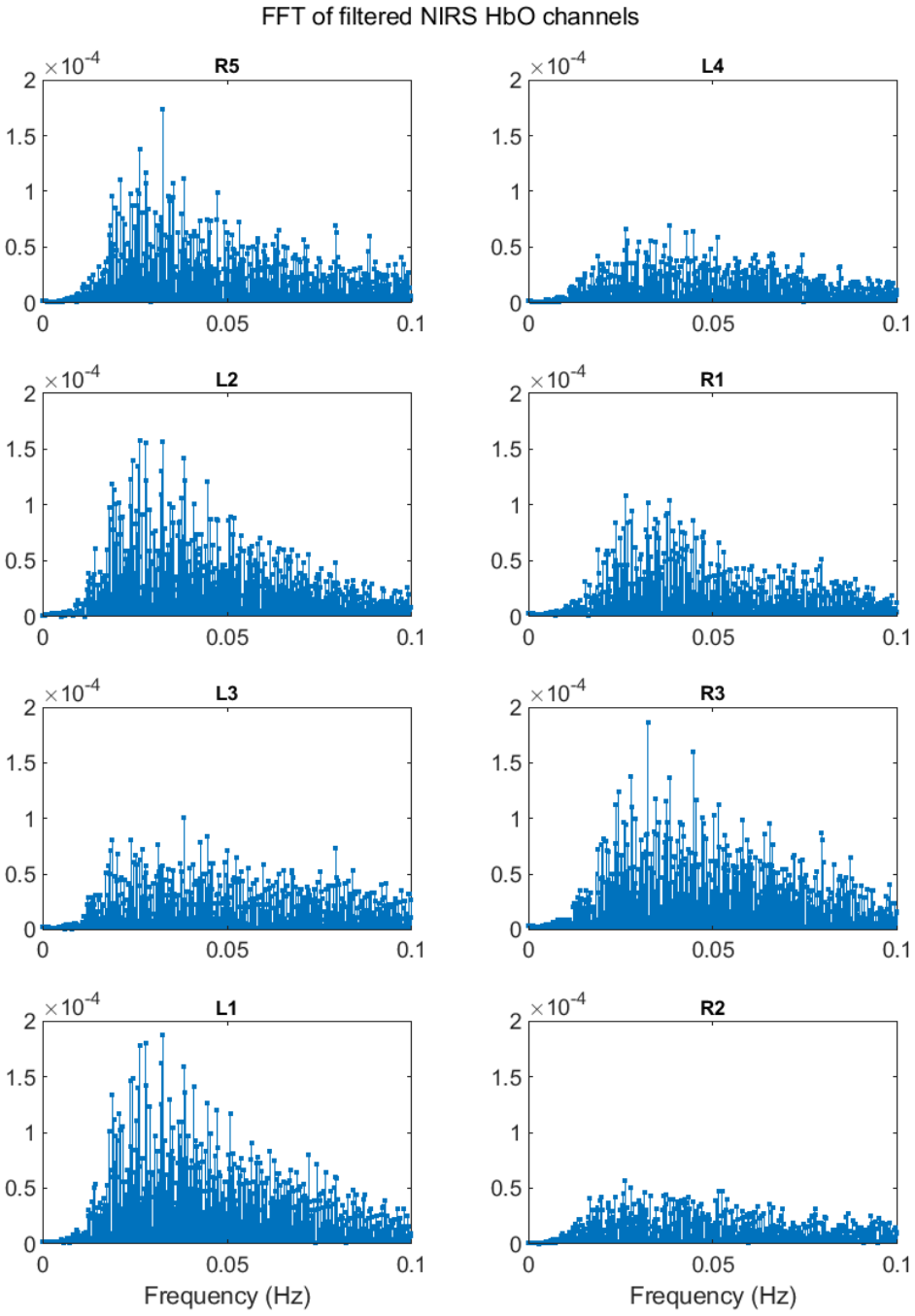

Figure 17: FFT of NIRS $\Delta[HbO_2]$. data per channel. The very low frequencies have been filtered out.

4.4 Spectrograms of NIRS $\Delta[HbO_2]$ and Δ[oxCCO] from each channel

Figures 18 to 21 show spectrograms for the NIRS $\Delta[HbO_2]$; the very low frequencies were filtered out.

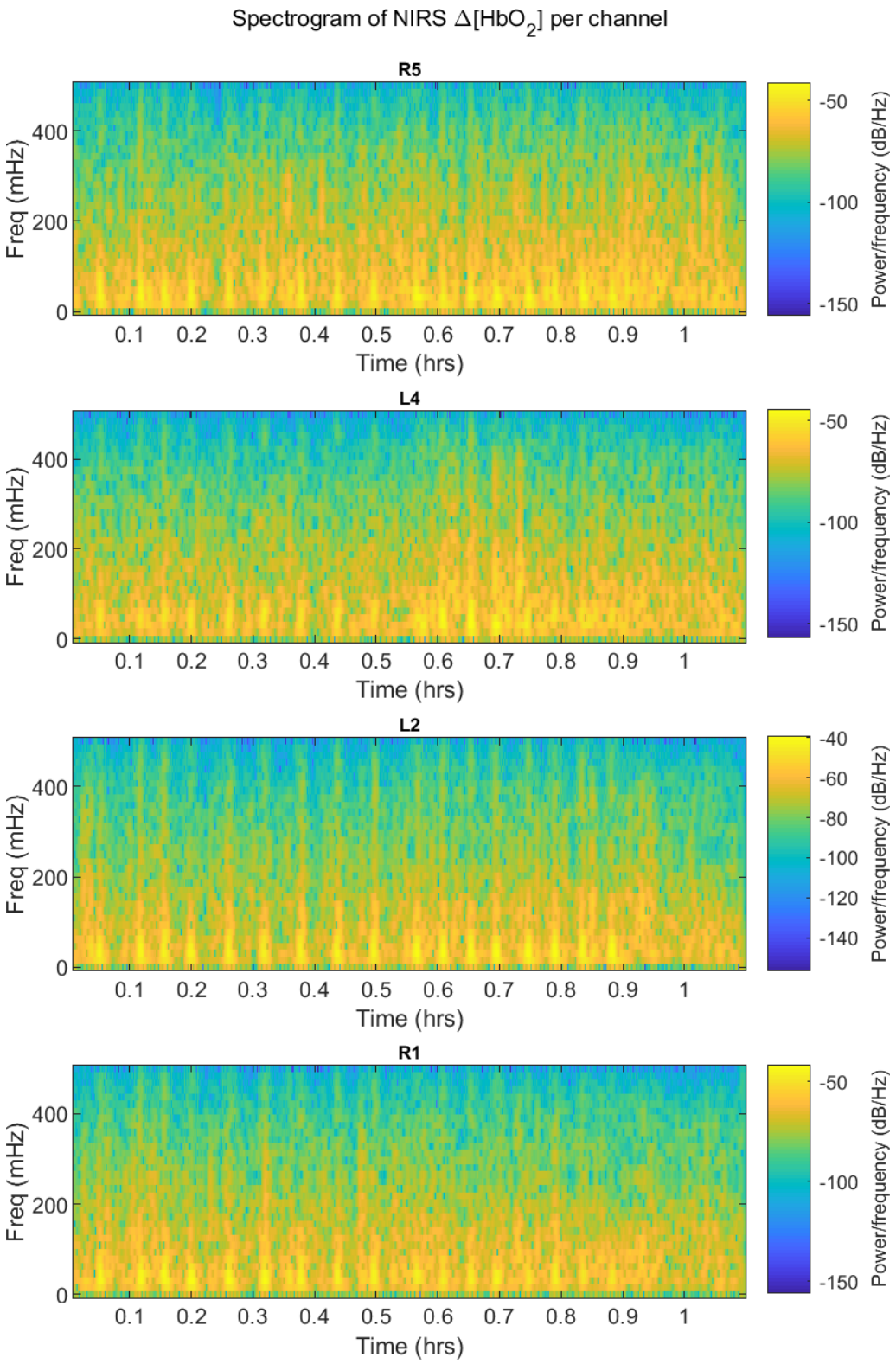

Figure 18: Spectrograms of NIRS $\Delta[\mathrm{HbO}_2]$.

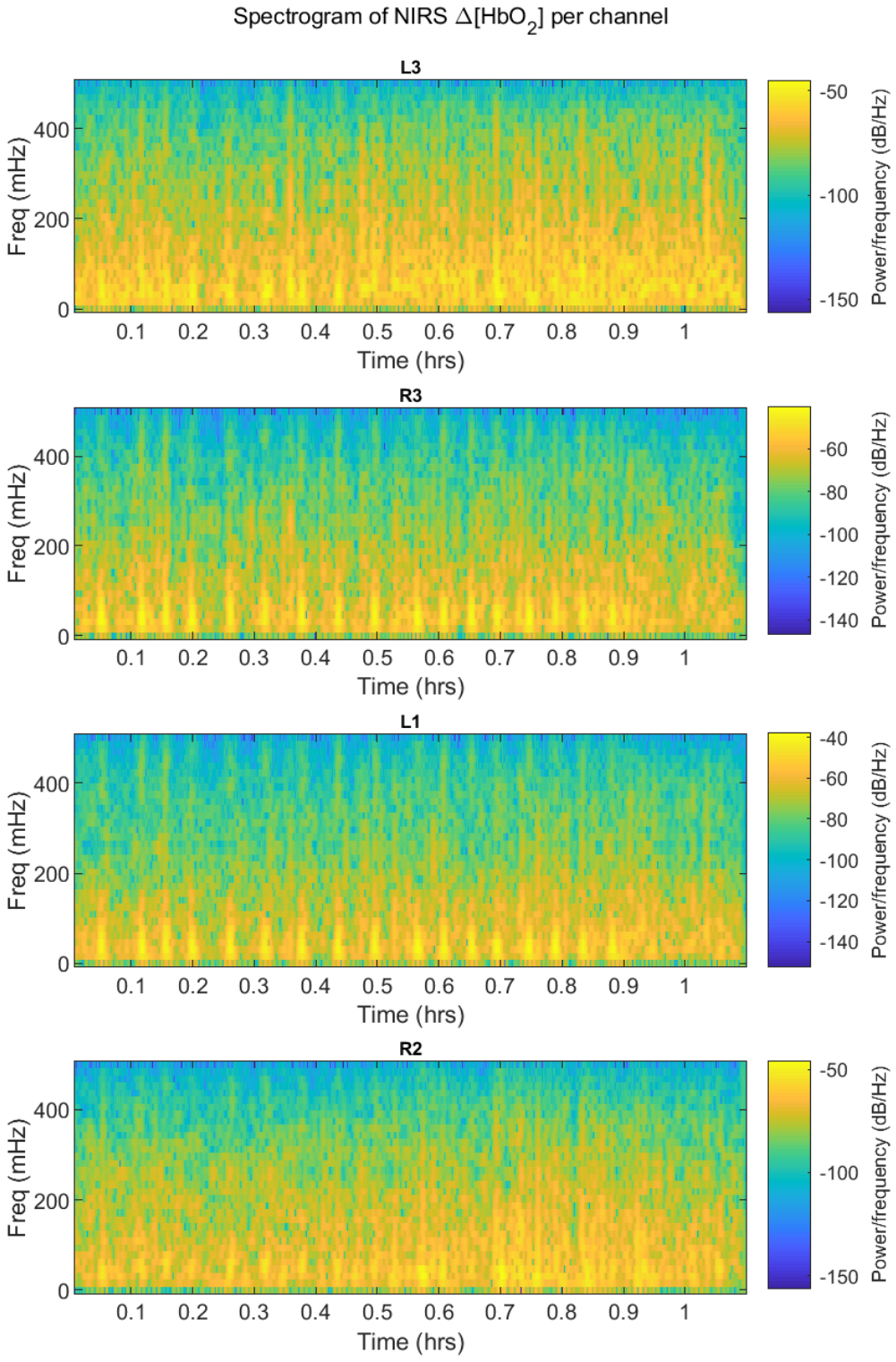

Figure 19: Spectrograms of NIRS $\Delta[\mathrm{HbO}_2]$.

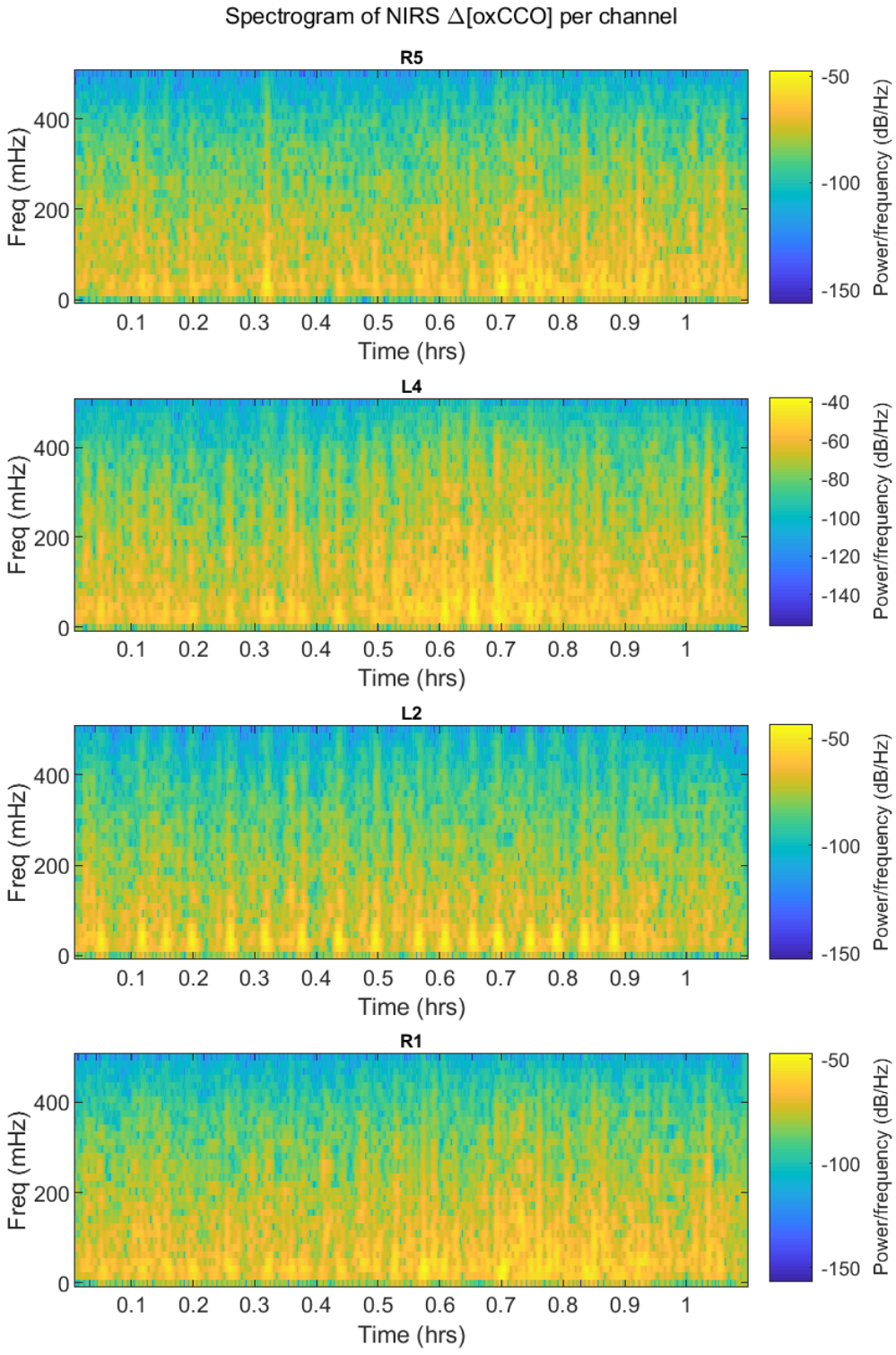

Figure 20: Spectrograms of NIRS Δ[oxCCO].

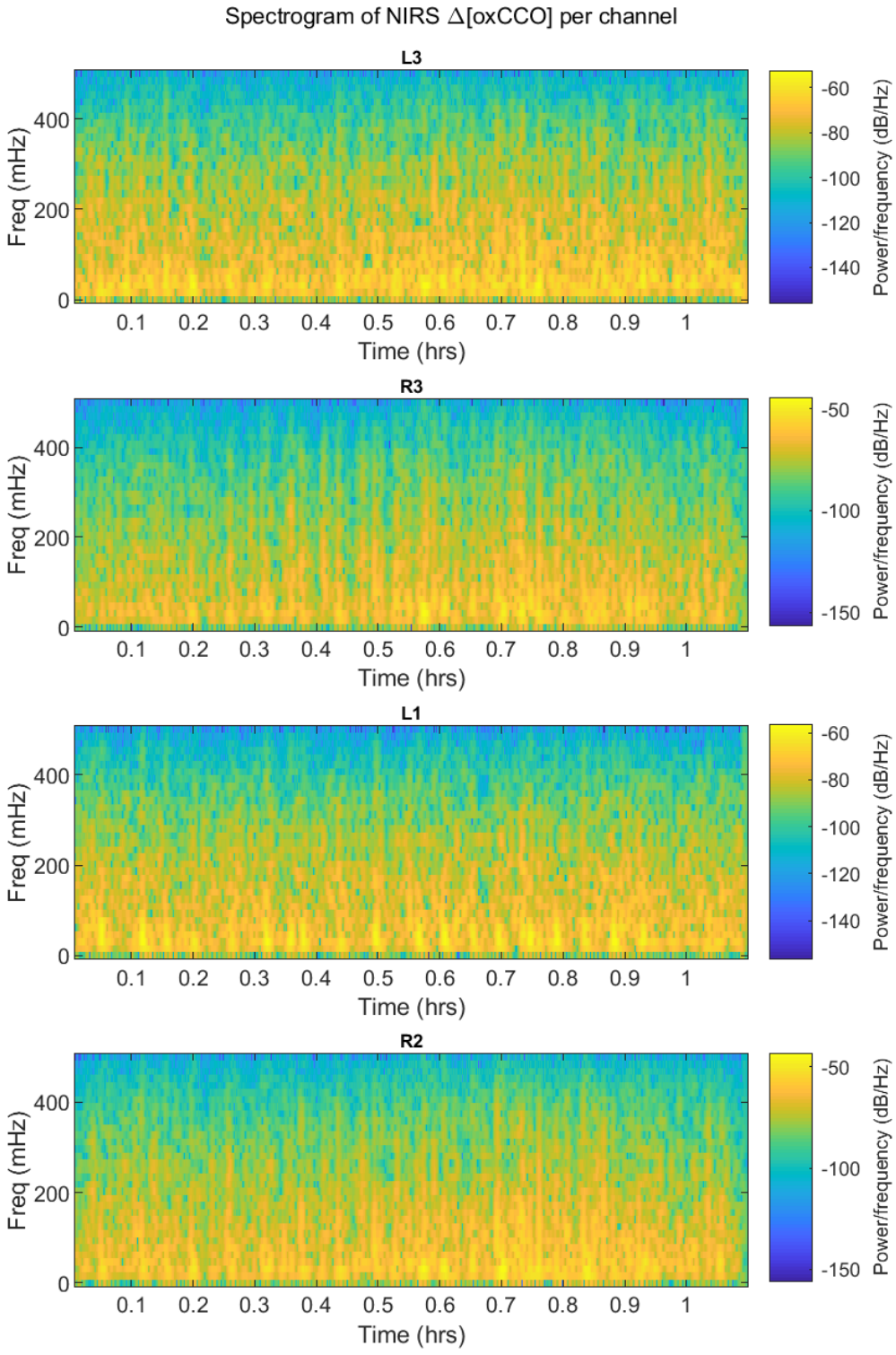

Figure 21: Spectrograms of NIRS Δ[oxCCO].

4.5 EEG seizure waveforms correlate with NIRS

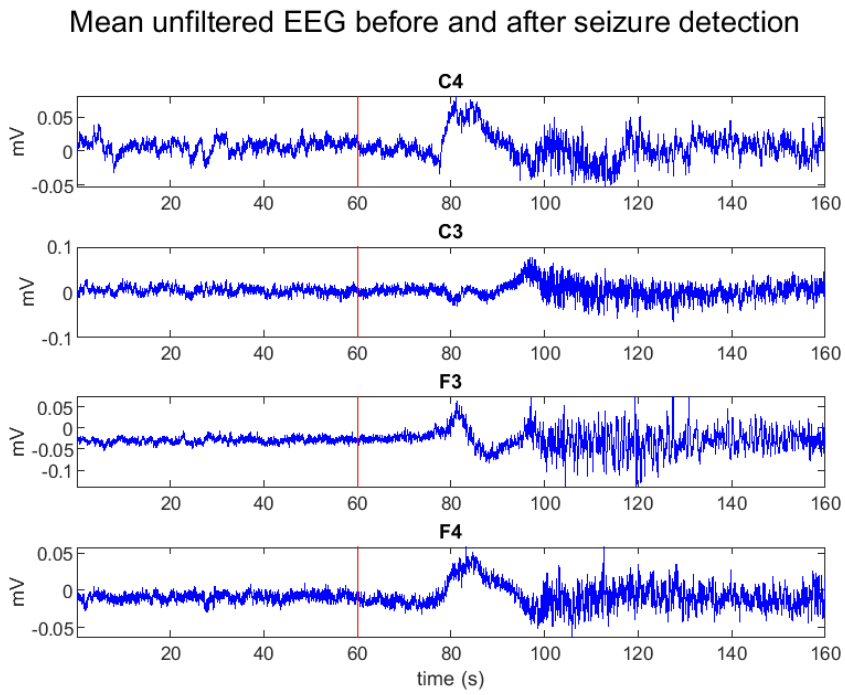

Figure 22: Mean unfiltered EEG before and after seizure detection (red line) per electrode location, 256Hz.

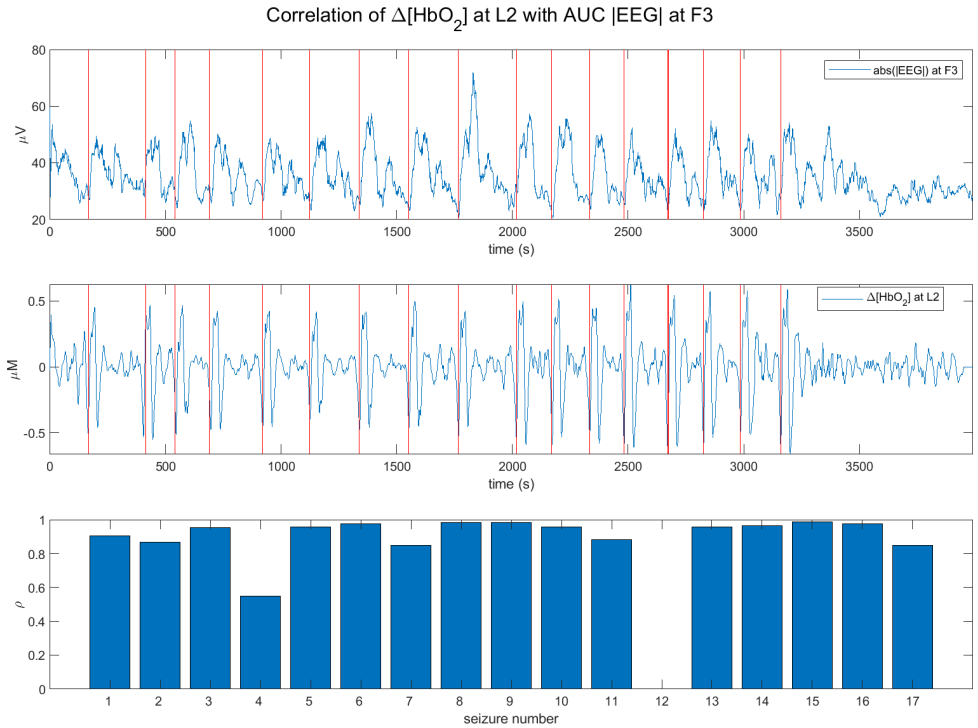

Figure 23: Correlation ρ of EEG at F3 with NIRS $\Delta[\mathrm{HbO}_2]$ at L2. Unfiltered EEG data, decimated to 1Hz, smoothed, each window phase shifted +21s $\pm$ {1,2}s, window 13s, relative to detection time (red line).

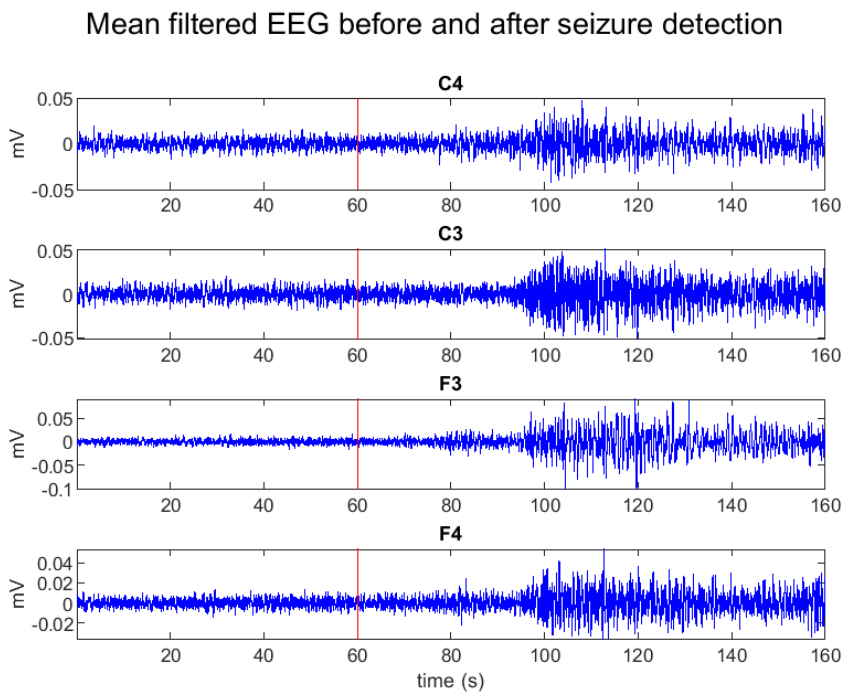

Figure 24: Mean filtered EEG before and after seizure detection (red line) per electrode location, 256Hz.

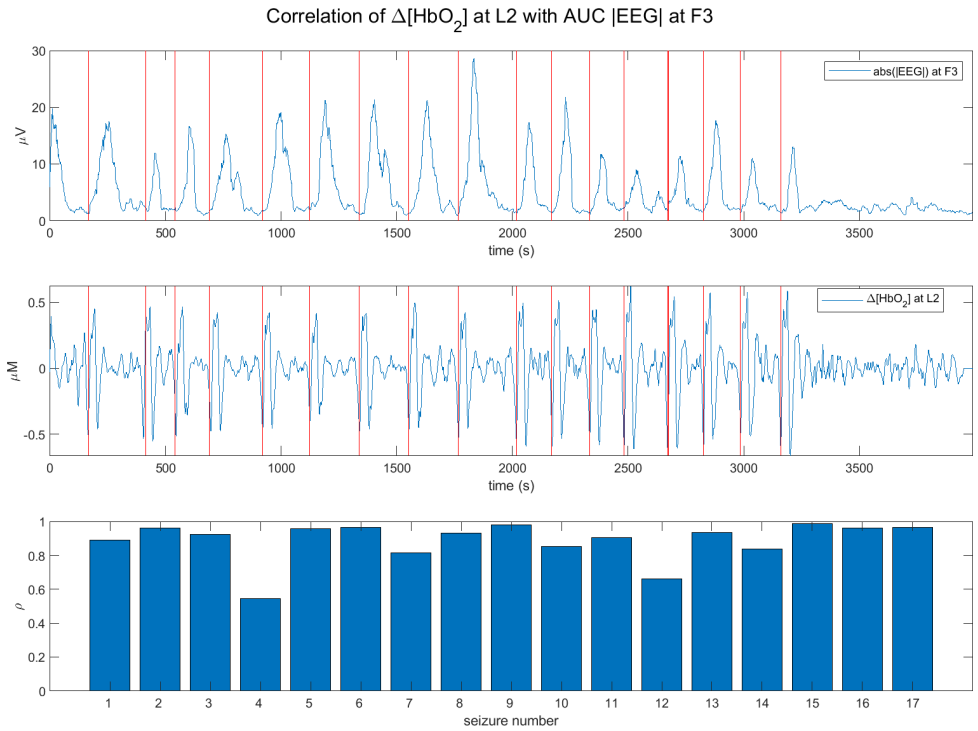

Figure 25: Correlation ρ of EEG at F3 with NIRS $\Delta[\mathrm{HbO}_2]$ at L2. Filtered EEG decimated to 1Hz, smoothed and each window phase shifted +36s $\pm$ {1,2}s, window 13s, relative to detection time (red line).

4.6 Mean NIRS seizure waveforms per channel

4.6.1 Mean peak aligned waveforms after seizure detection

For each channel and for each seizure, the five NIRS waveforms were peak aligned relative to the after detection time window. Waveforms that peaked before the mid point of the time window were shifted left by negative seconds, waveforms that peaked after the mid point were shifted right by positive seconds. Mean and standard deviation of the shifts, in seconds (rounded), for each waveform are in Table 1, waveforms are in Figures 26 to 29.

	$\Delta[HbO_2]$		Δ[HHb]		Δ[HbT]		Δ[HbD]		Δ[oxCCO]	
	μ	σ	μ	σ	μ	σ	μ	σ	μ	σ
R5	-2	4	7	3	0	4	-2	4	-3	4
L4	-3	4	3	5	2	4	-4	7	-8	5
L2	-2	4	5	4	2	4	-3	4	-1	3
R1	-3	4	7	4	2	5	-3	4	-5	3
L3	-4	4	4	6	-1	8	-3	4	-6	6
R3	-3	4	5	5	-2	5	-2	4	-6	4
L1	-2	4	5	4	1	4	-3	4	0	4
R2	1	10	7	3	7	8	-2	7	-5	3

Table 1: Wave alignment: μ is the mean number of seconds (rounded) the waveforms were shifted to align their peaks. Waveforms that peaked early were shifted left by negative seconds, waveforms that peaked late were shifted right by positive seconds. σ is the standard deviation of the shift values.

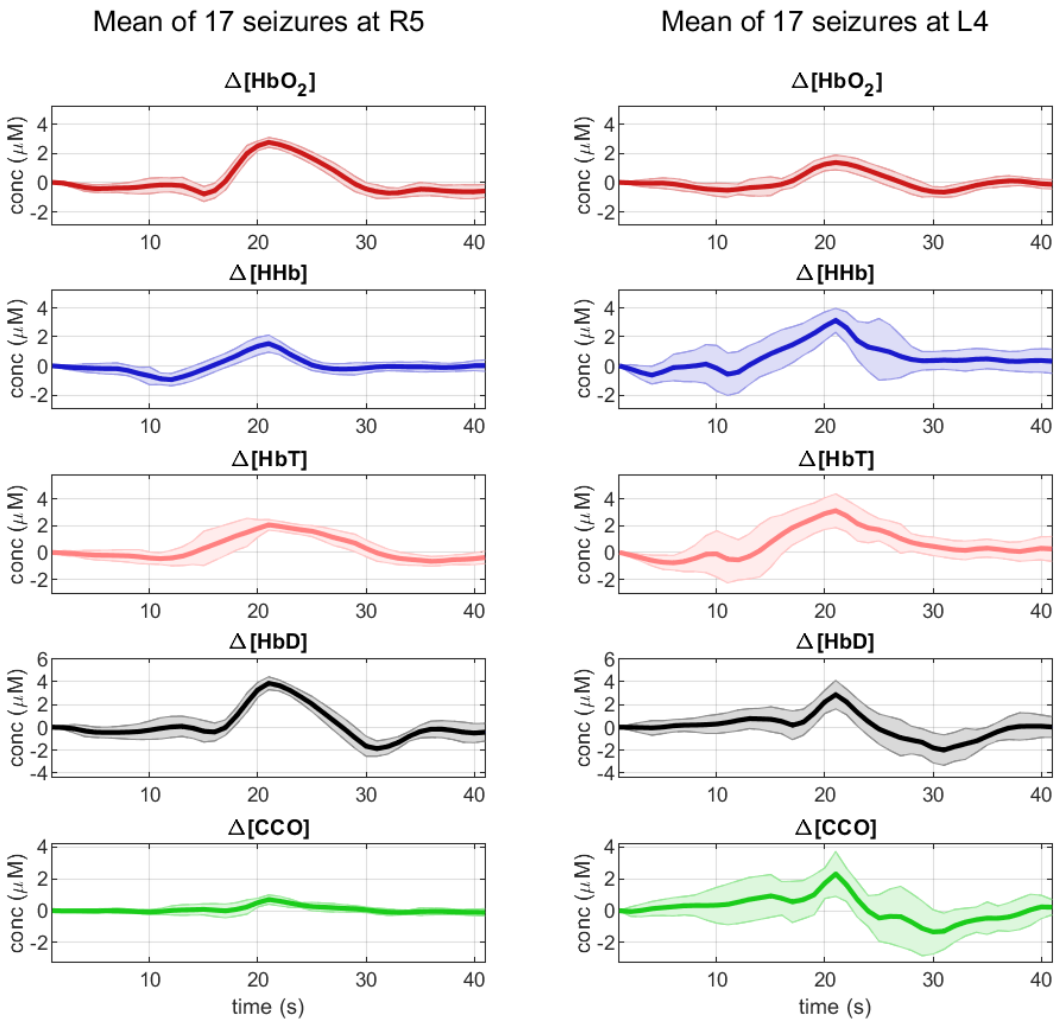

(a) (b)

Figure 26: Mean **peak aligned** Δ[Hb] and Δ[oxCCO] after detection.

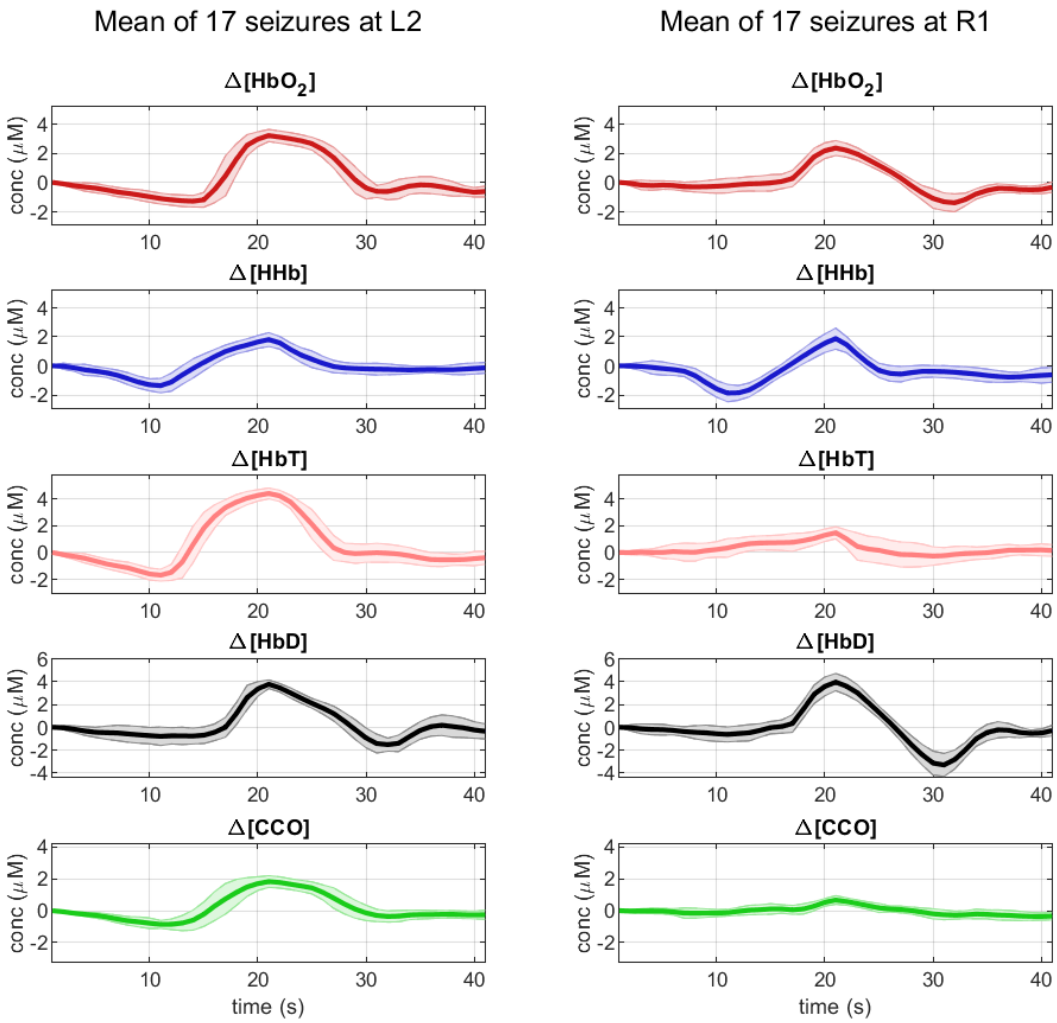

(a) (b)

Figure 27: Mean **peak aligned** Δ[Hb] and Δ[oxCCO] after detection.

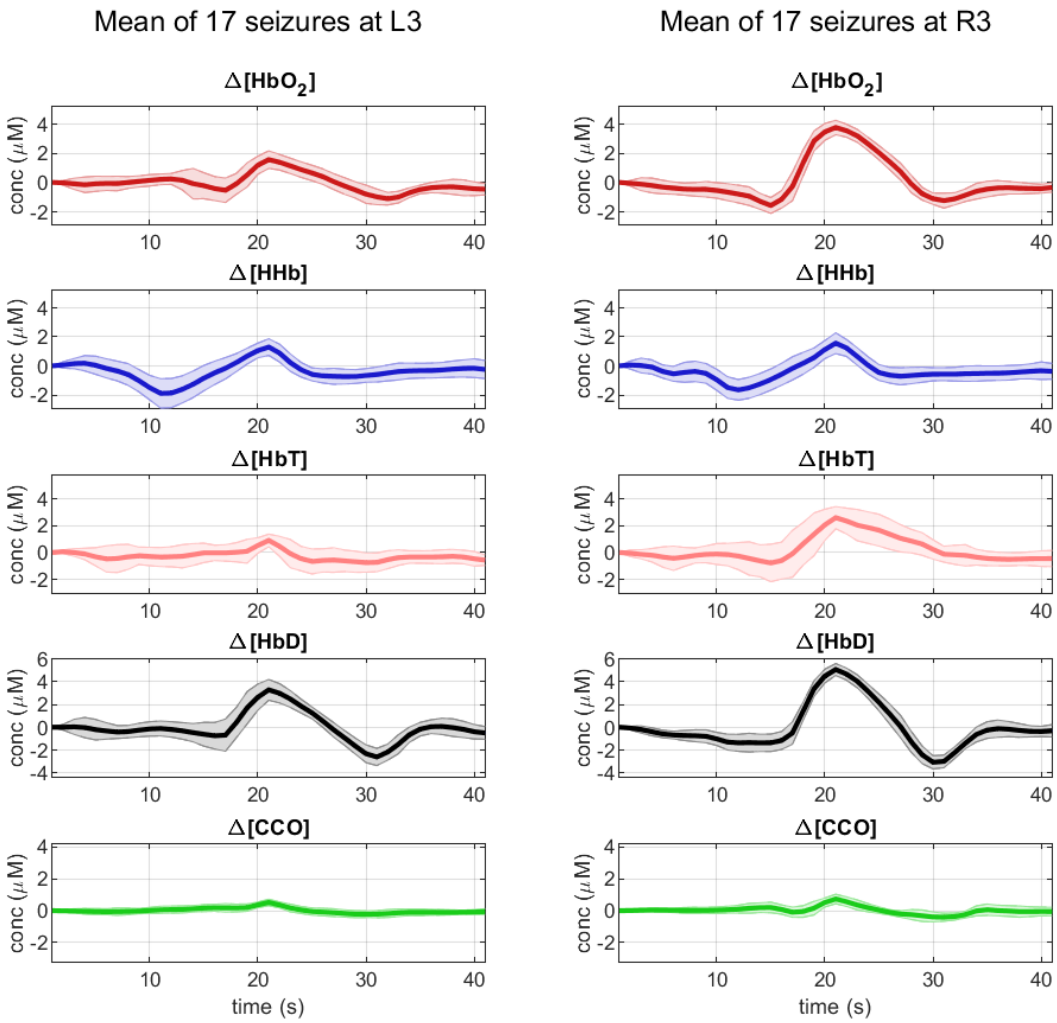

(a) (b)

Figure 28: Mean **peak aligned** Δ[Hb] and Δ[oxCCO] after detection.

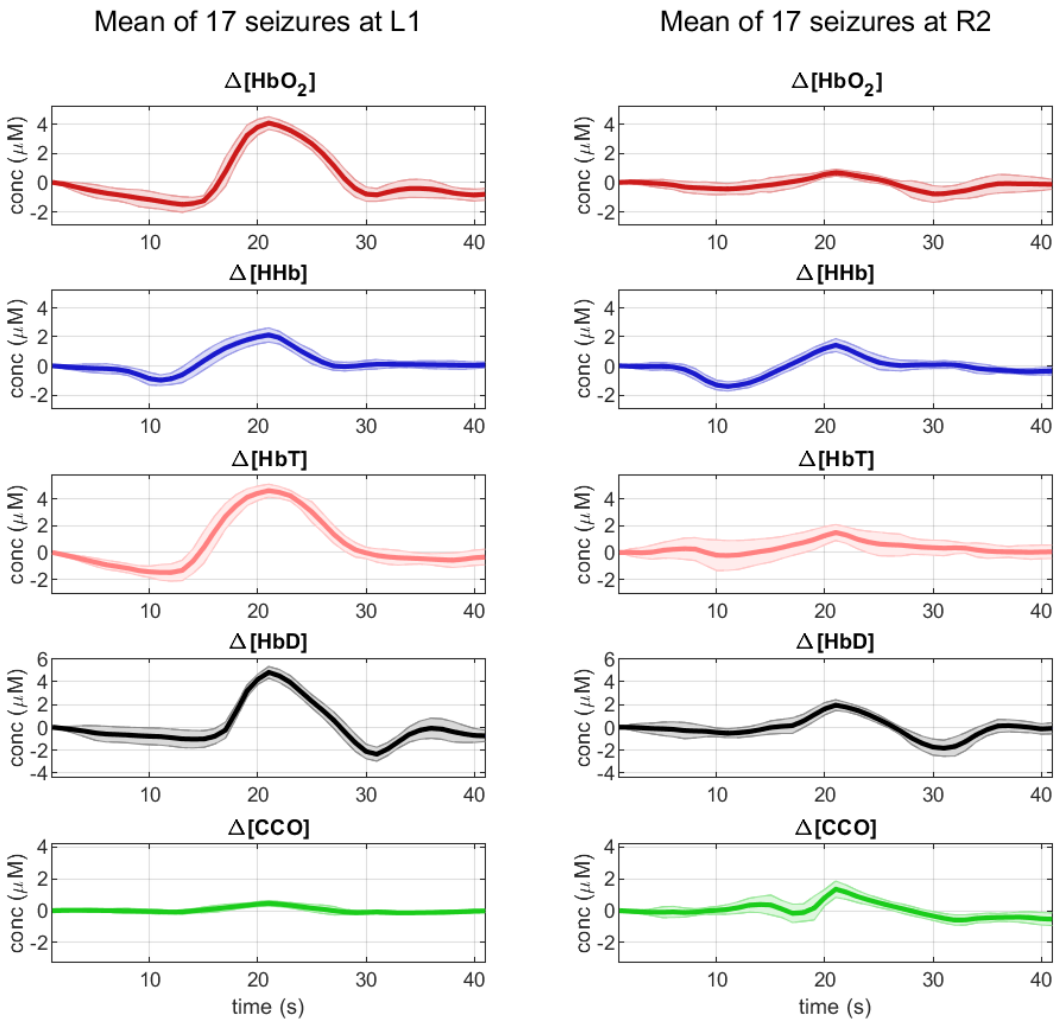

(a) (b)

Figure 29: Mean **peak aligned** Δ[Hb] and Δ[oxCCO] after detection.

4.6.2 Mean seizure detection aligned changes in [Hb] and [oxCCO]

Figures 30 to 33 show mean detection time aligned waveforms. Each waveform is the mean for the 40s after 17 detection times per channel.

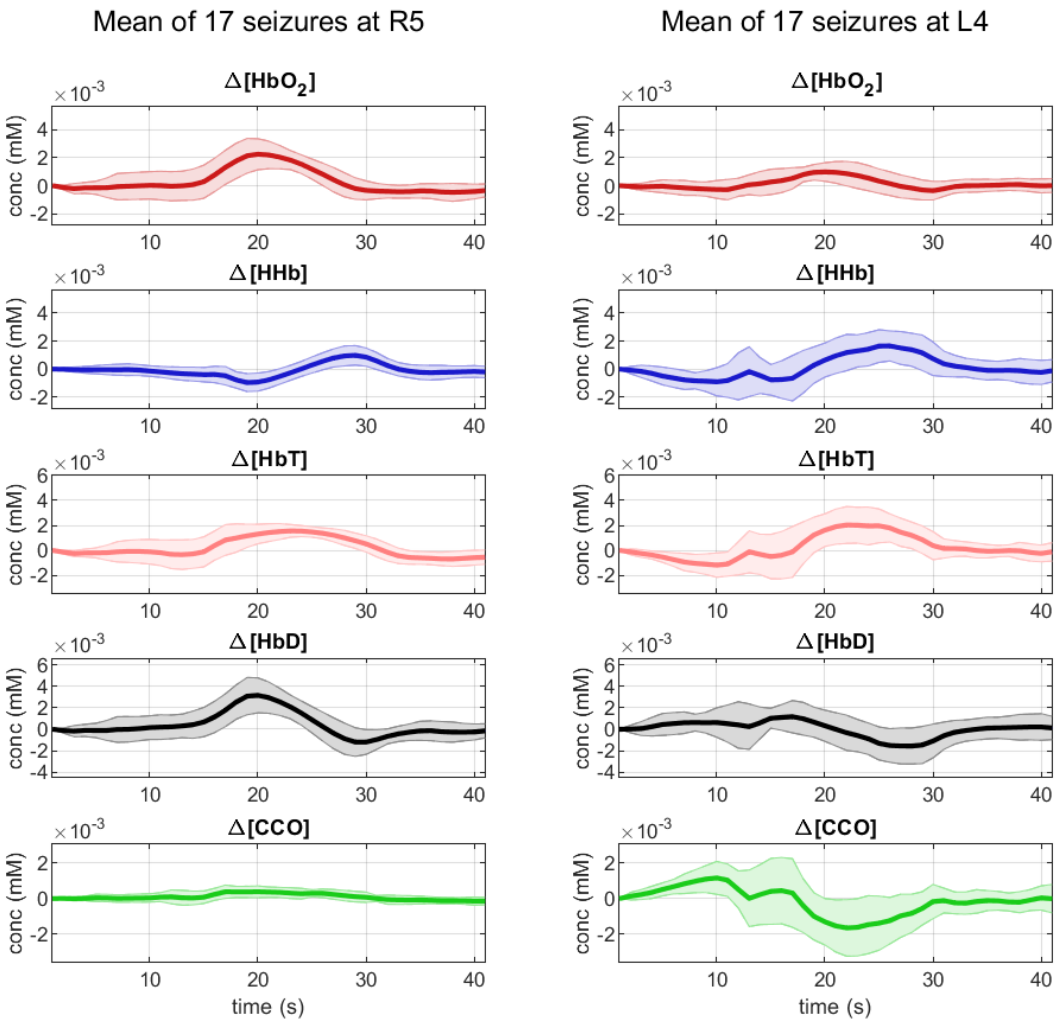

(a) (b)

Figure 30: Mean **detection aligned** Δ[Hb] and Δ[oxCCO] after detection.

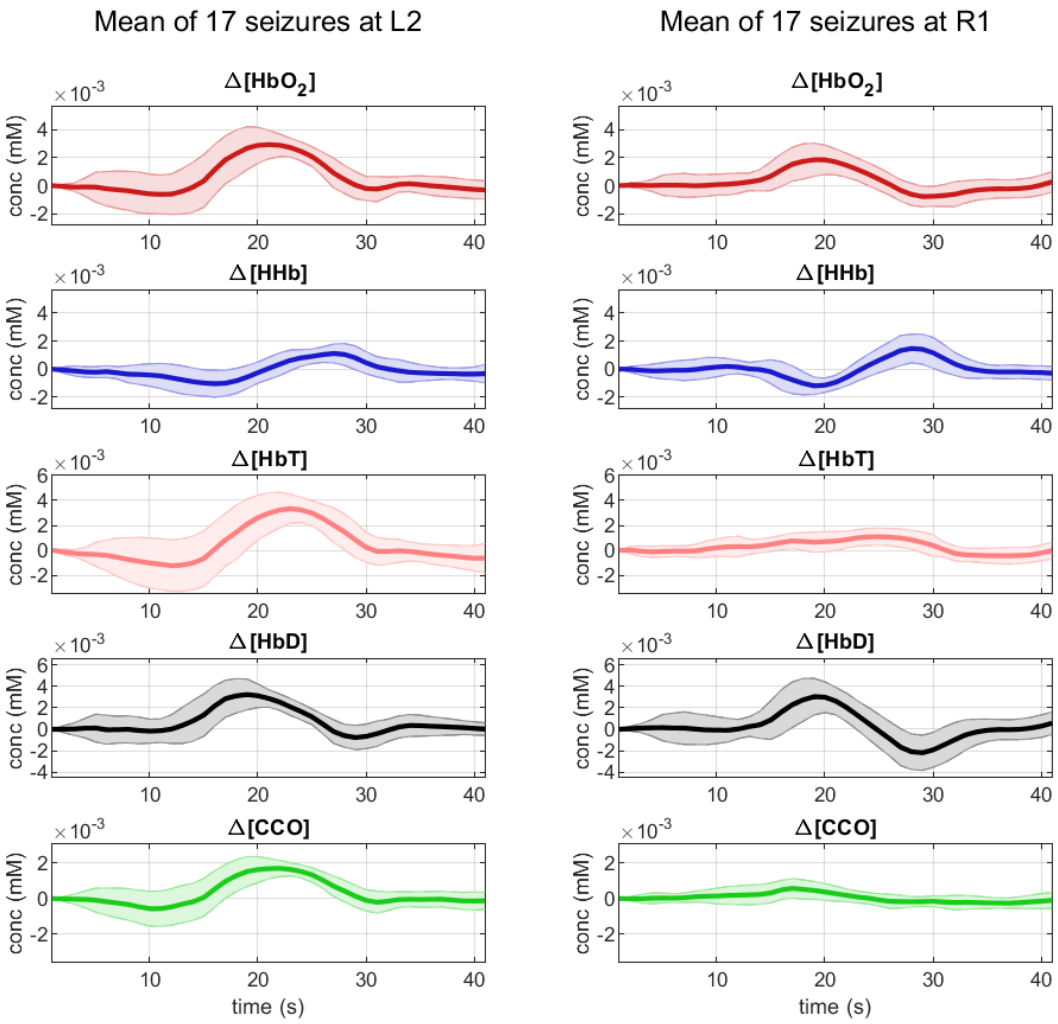

(a) (b)

Figure 31: Mean **detection aligned** Δ[Hb] and Δ[oxCCO] after detection.

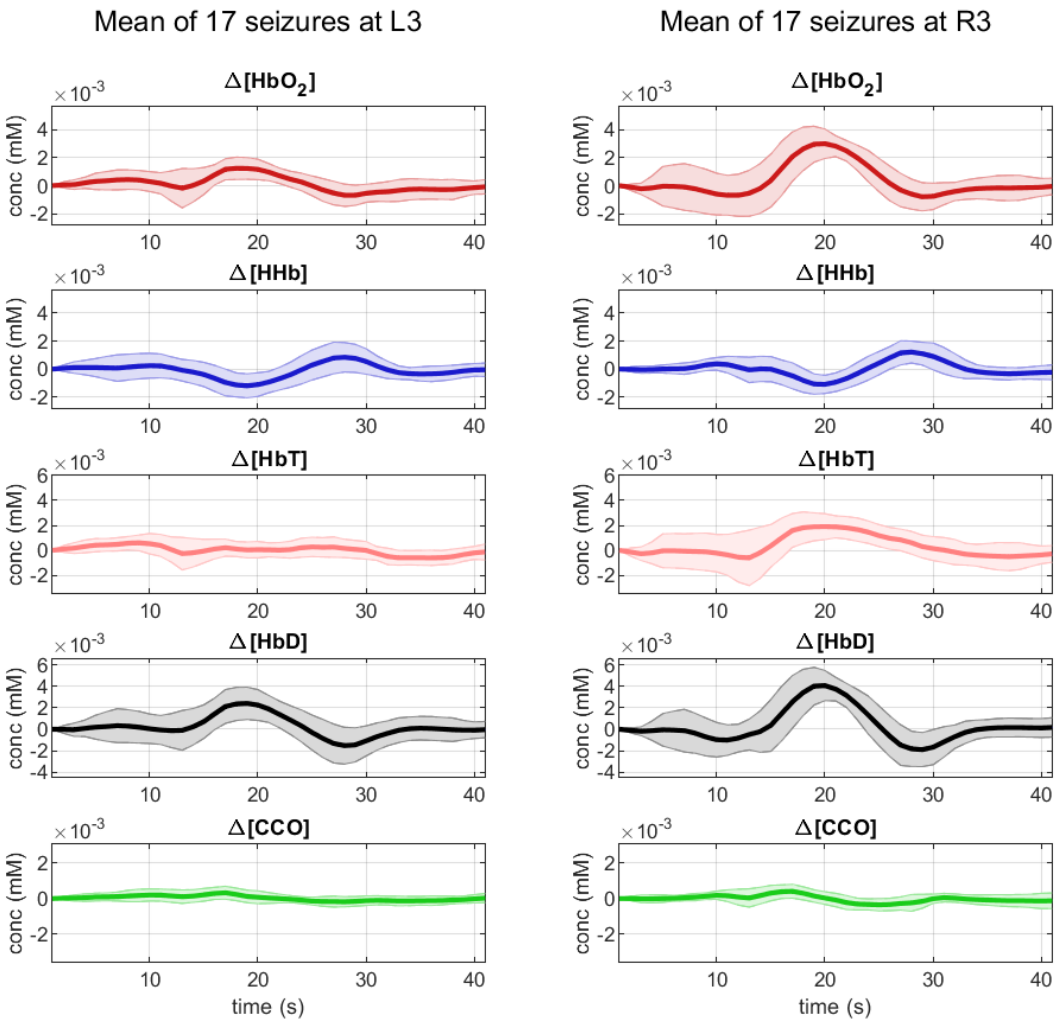

(a) (b)

Figure 32: Mean **detection aligned** Δ[Hb] and Δ[oxCCO] after detection.

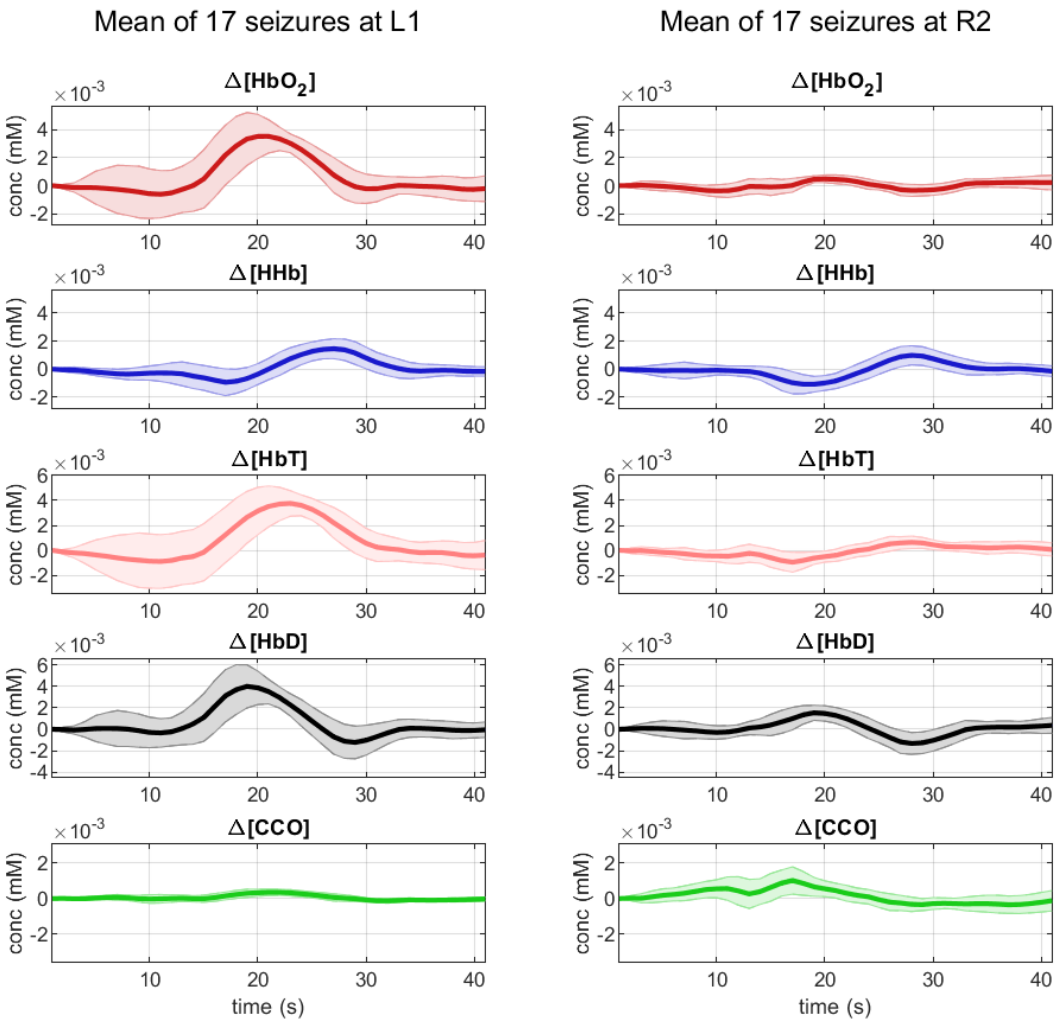

(a) (b)

Figure 33: Mean **detection aligned** Δ[Hb] and Δ[oxCCO] after detection.

4.6.3 Correlation of each EEG with all NIRS channels before and after seizure detection

The bar charts in Figures 34, 35, 36, 37 show the correlation of four EEG traces with Δ[Hb] and Δ[oxCCO] at each NIRS channel during 40s before and after detection.

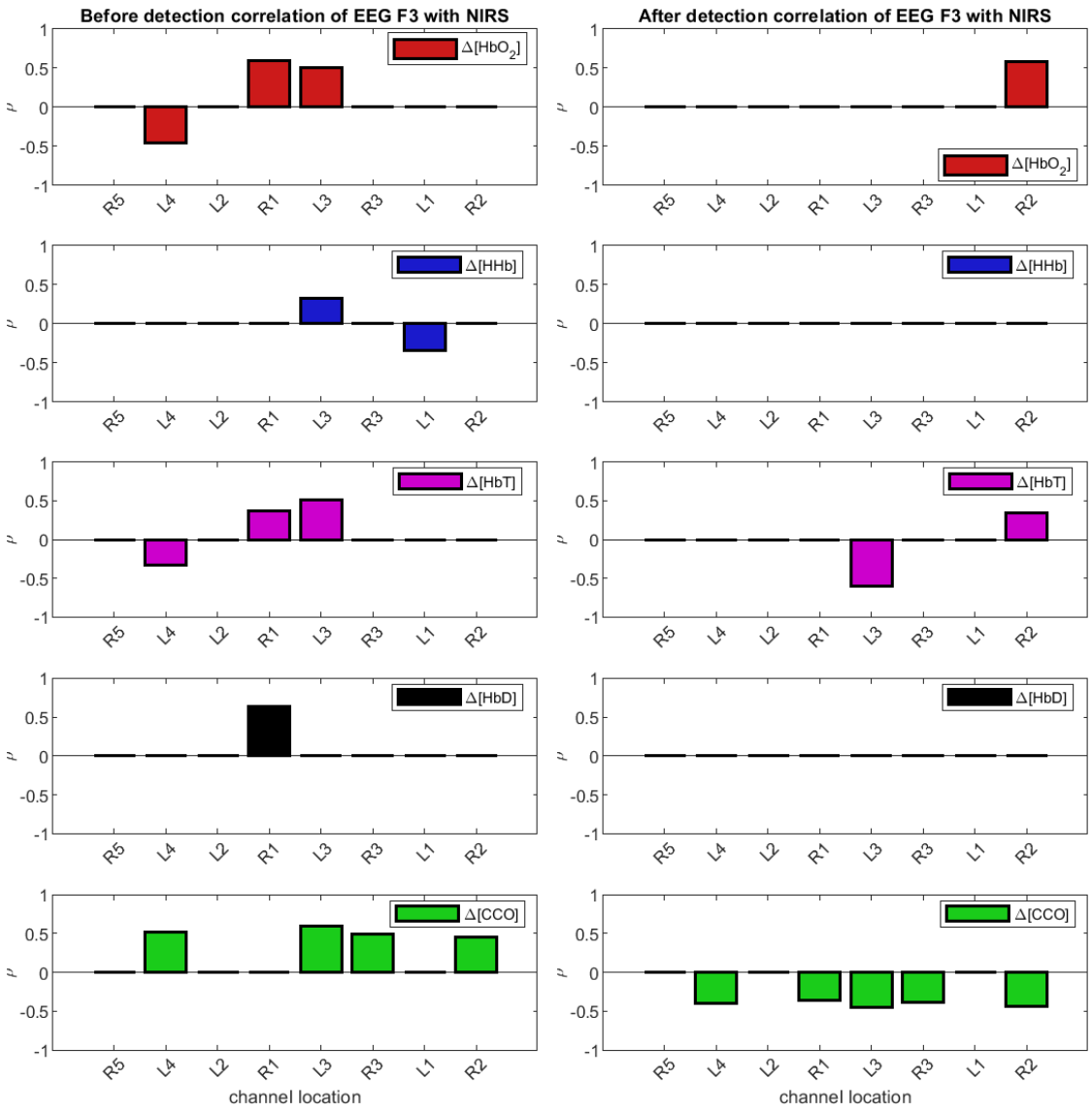

(a) ρ during 40s before detection (b) ρ during 40s after detection

Figure 34: Correlation of EEG F3 with NIRS at eight locations.

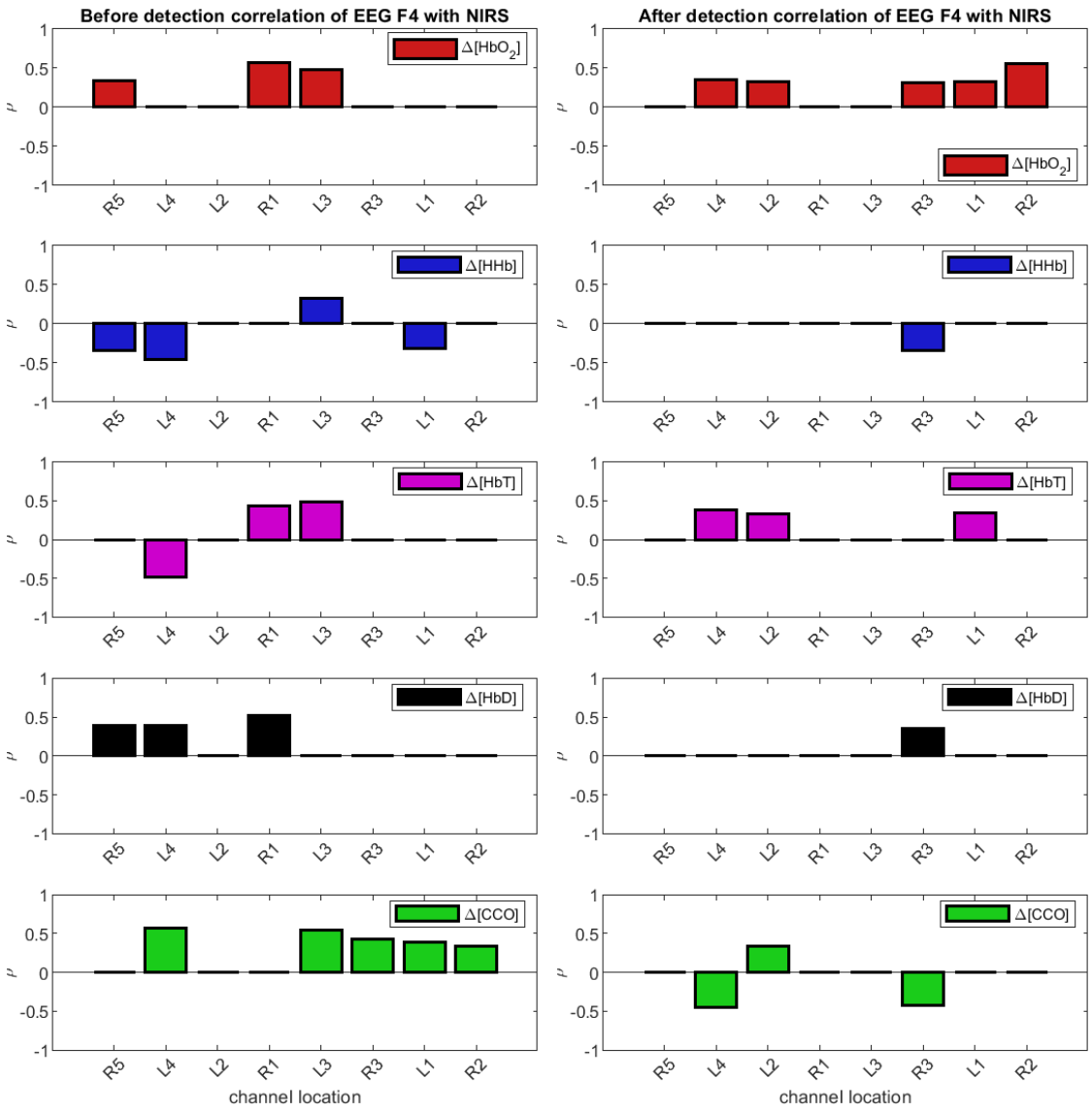

(a) ρ during 40s before detection (b) ρ during 40s after detection

Figure 35: Correlation of EEG F4 with NIRS at eight locations.

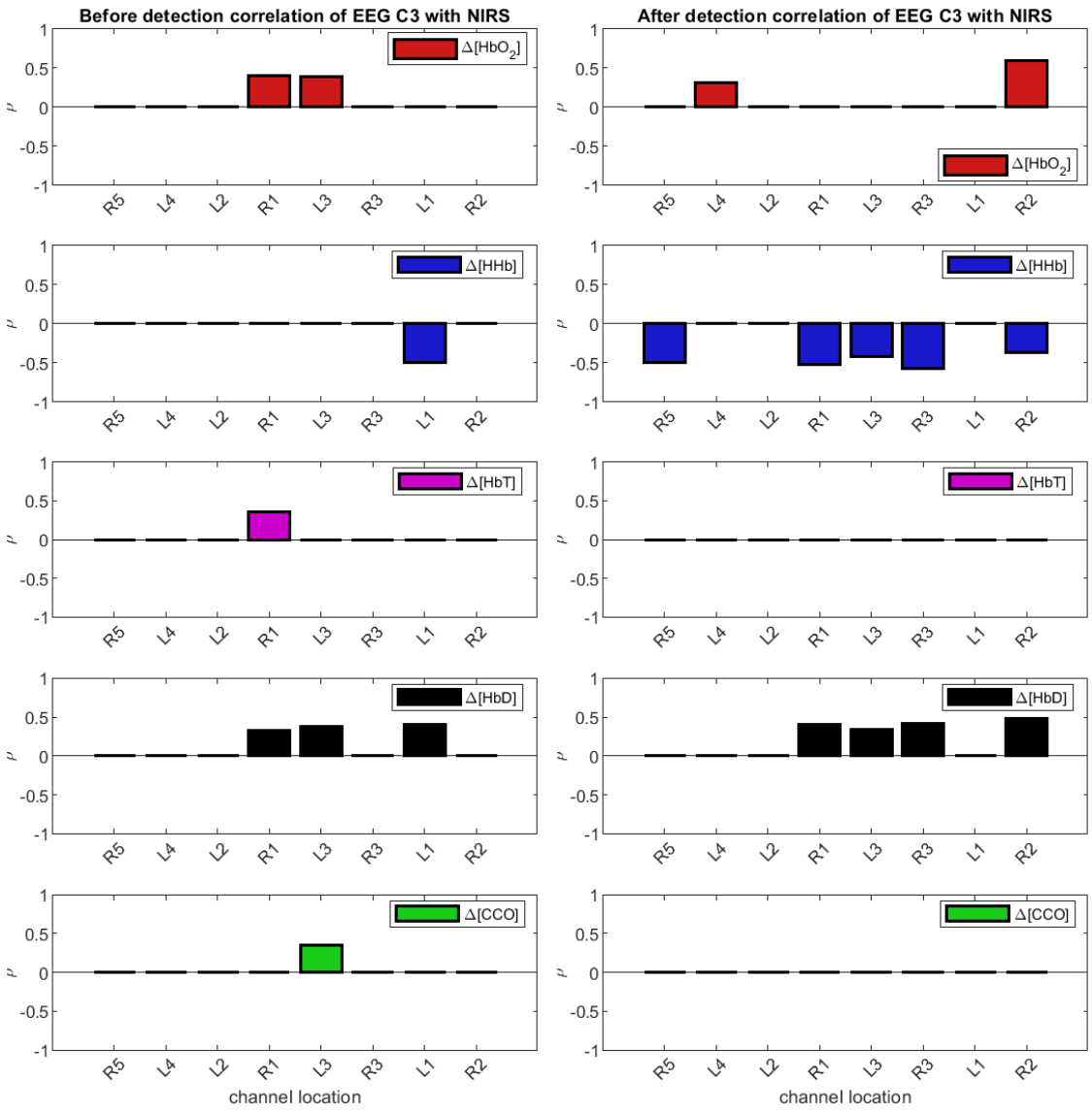

(a) ρ during 40s before detection (b) ρ during 40s after detection

Figure 36: Correlation of EEG C3 with NIRS at eight locations.

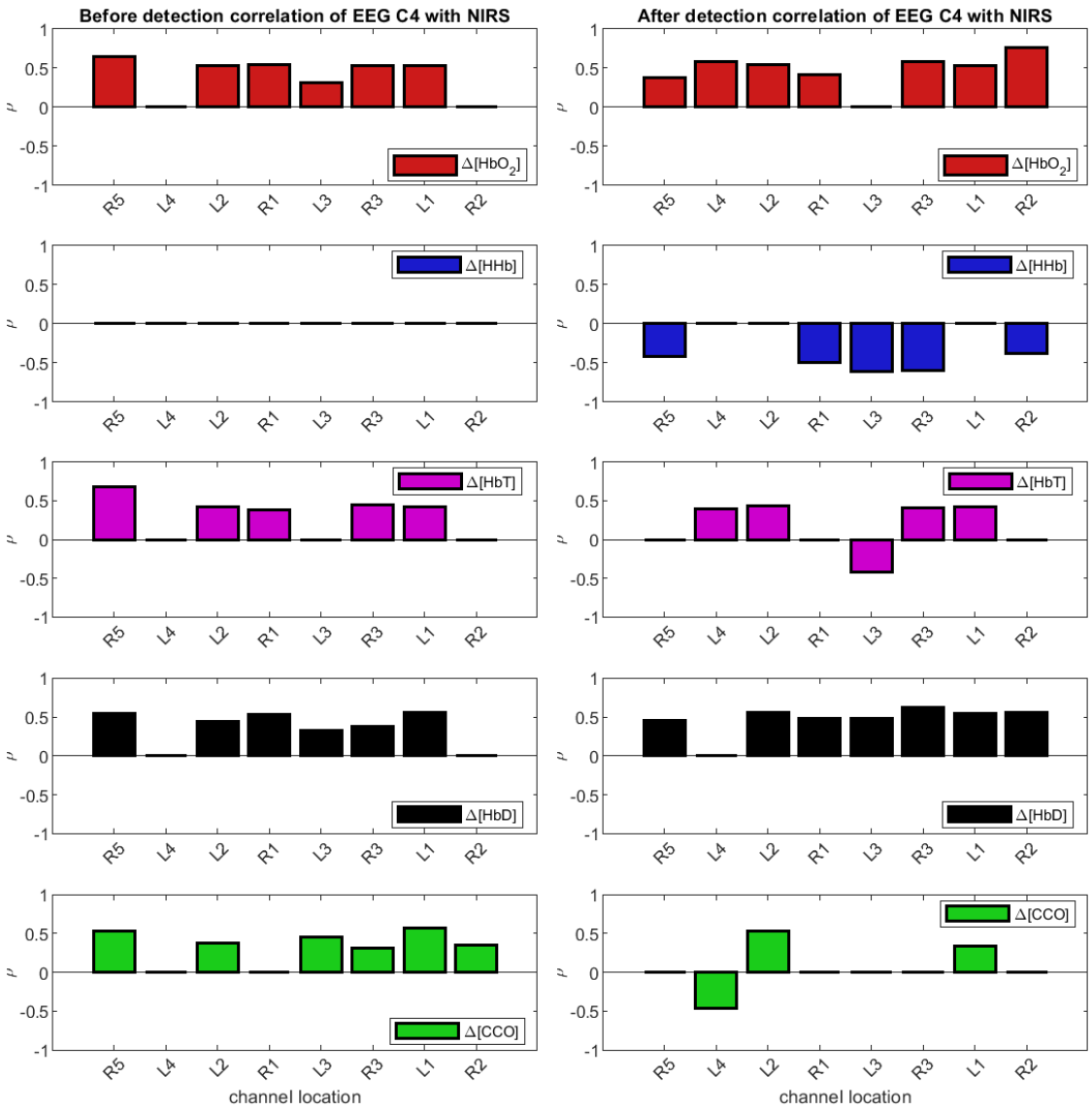

(a) ρ during 40s before detection (b) ρ during 40s after detection

Figure 37: Correlation of EEG C4 with NIRS at eight locations.

4.6.4 Correlation of each EEG with a proximate NIRS channel

Figure 38 shows the correlation of each EEG with proximate NIRS channels 40s before and after seizure detection.

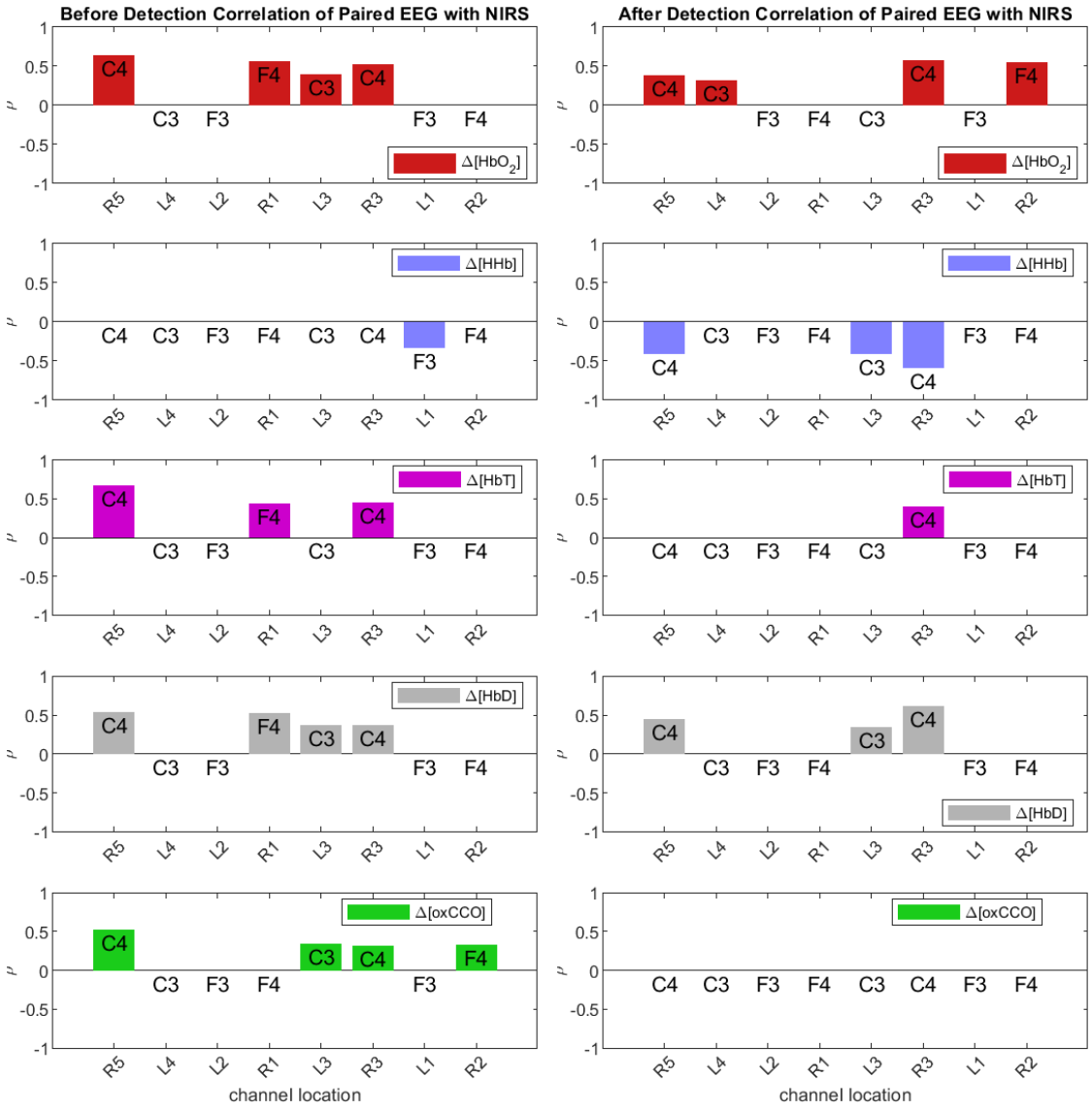

(a) correlation 40s before detection (b) correlation 40s after detection

Figure 38: Correlation coefficients of each EEG with proximate NIRS channels.

4.6.5 Correlation of Δ[Hb] with Δ[oxCCO] before and after seizure detection

Figure 39 shows the correlation of mean Δ[Hb] with mean Δ[oxCCO during 40s before versus after detection.

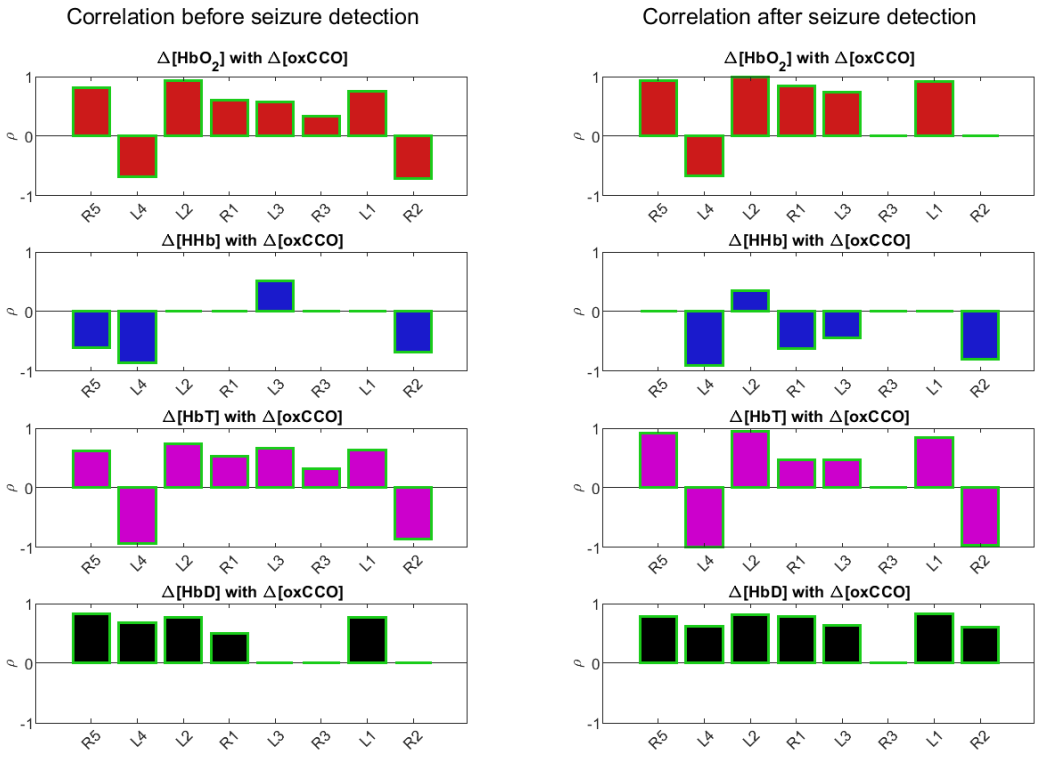

(a) ρ during 40s before detection

(b) ρ during 40s after detection

Figure 39: Correlation of Δ[Hb] with Δ[oxCCO] at eight NIRS locations.

4.6.6 Correlation of Δ[oxCCO] with Δ[Hb] during a sliding time window

In the following figures seizures are indicated by shaded areas. Correlation was calculated with a sliding window 30s wide, then smoothed using a 30 second window.

- Figures 40 and 41: correlation of Δ[oxCCO] with Δ[Hb] at locations R1, R2, R3 and R5.
- Figures 42 and 43: correlation of Δ[oxCCO] with Δ[Hb] at locations L1, L2, L3 and L4.

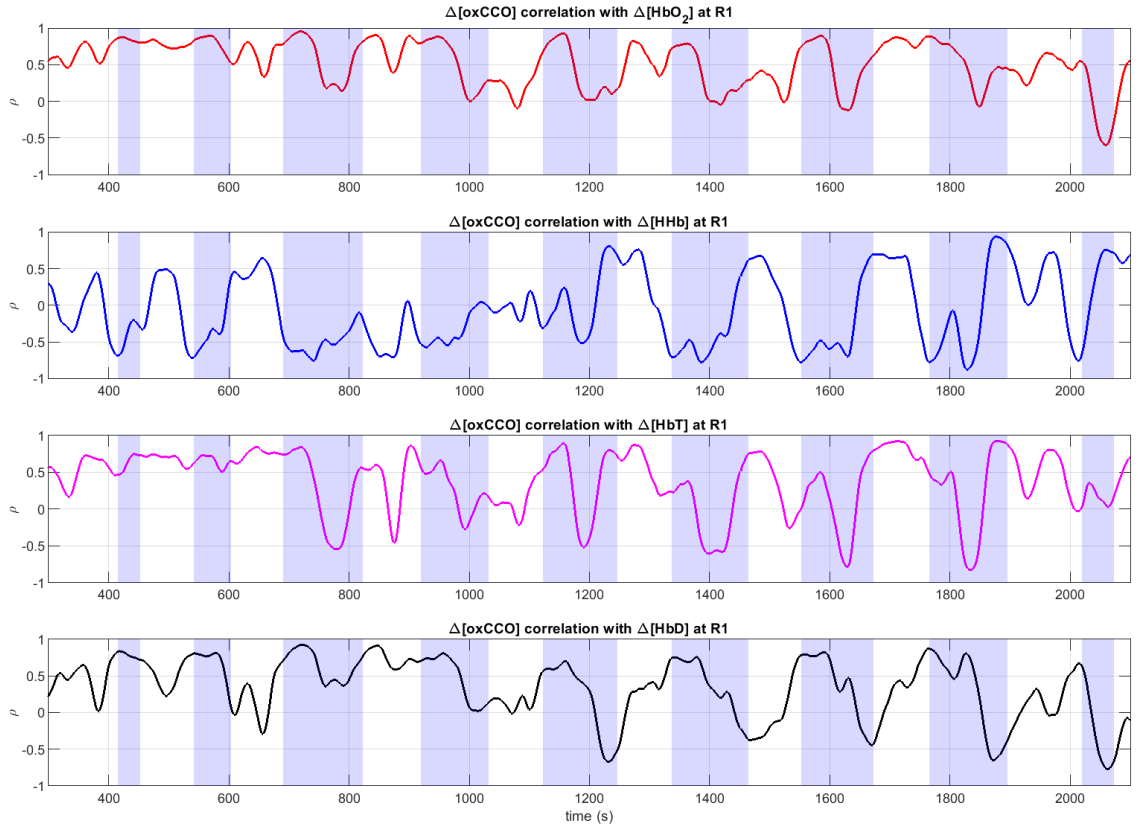

(a) R1

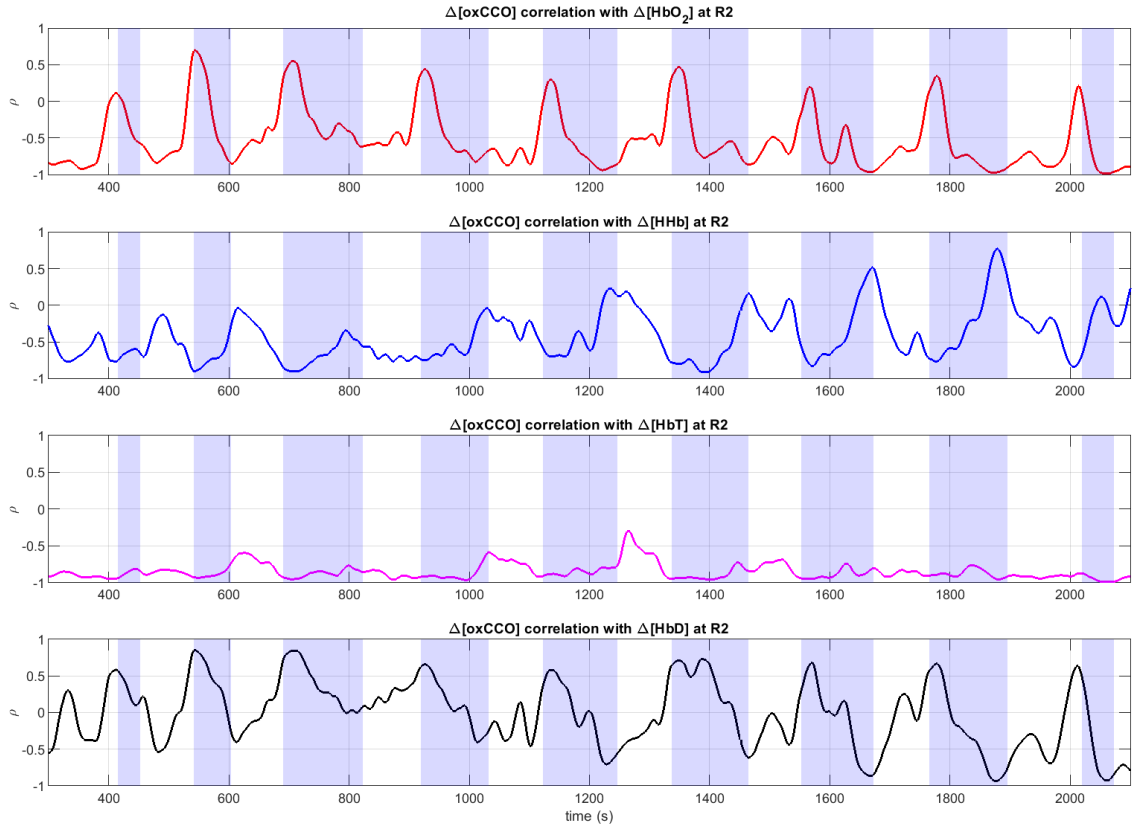

(b) R2

Figure 40: Δ[oxCCO] correlation with Δ[Hb].

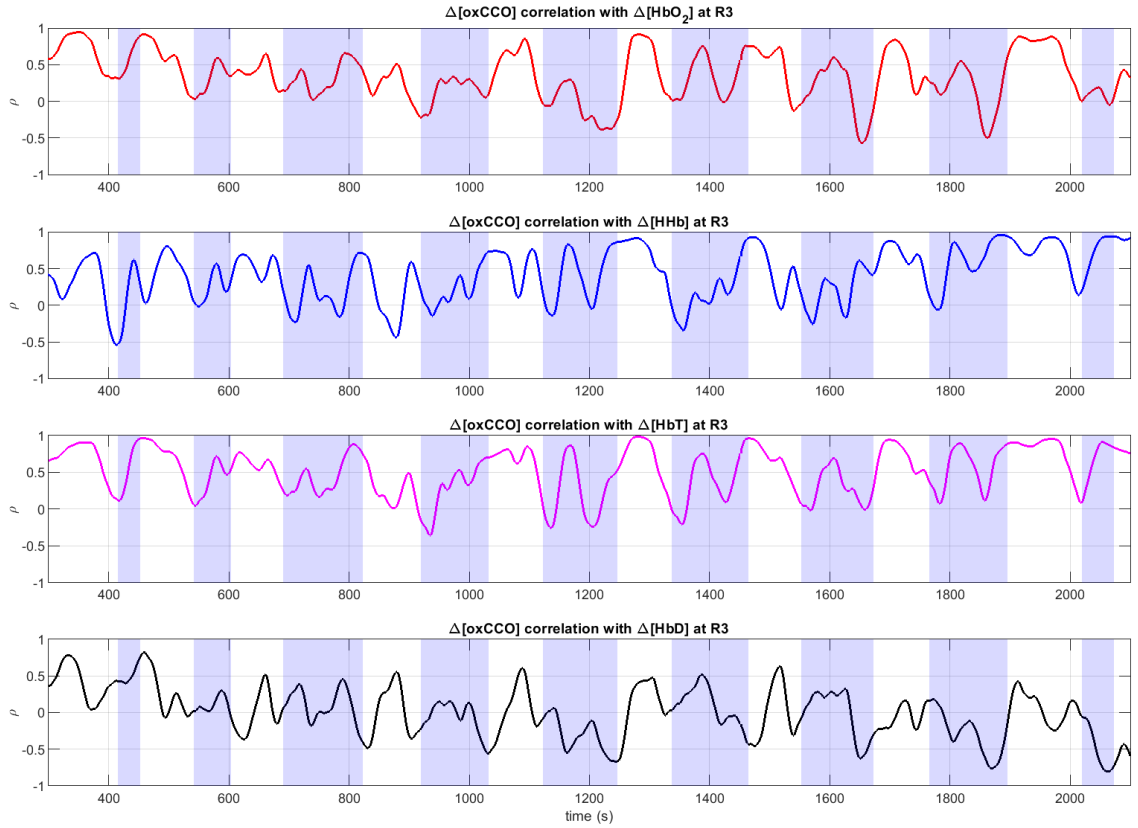

(a) R3

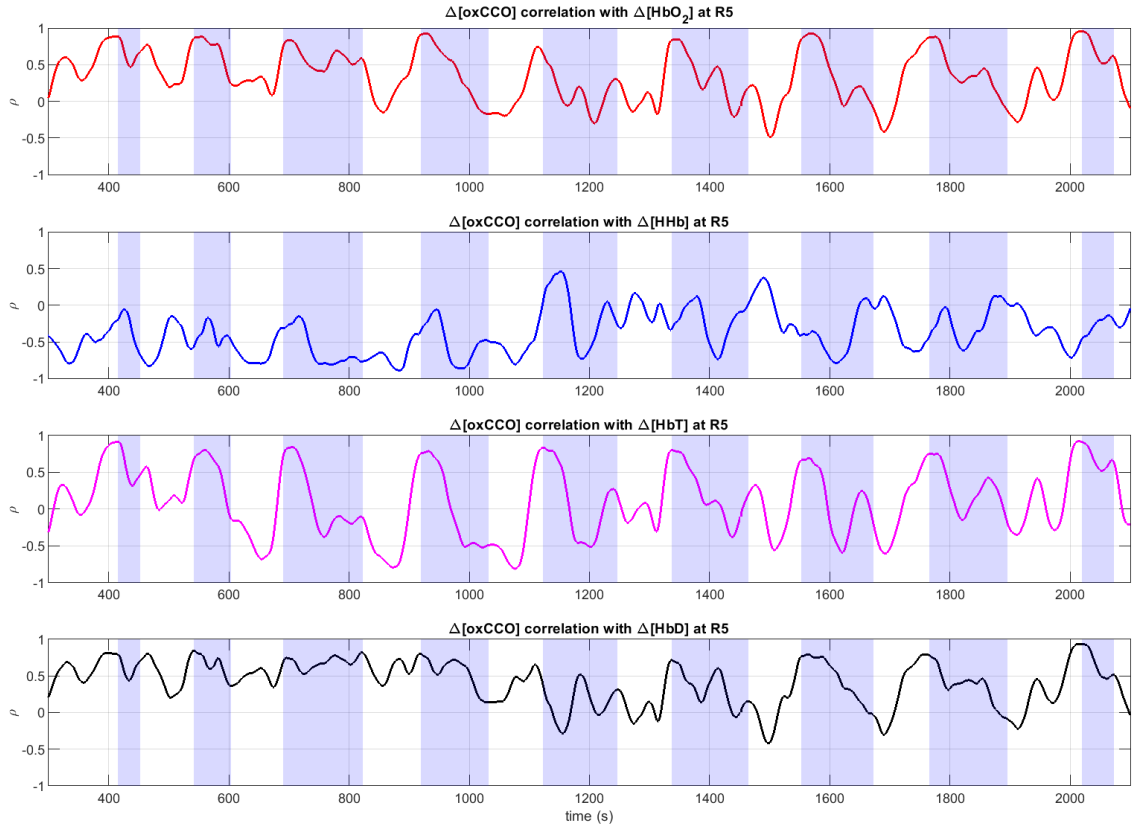

(b) R5

Figure 41: Δ[oxCCO] correlation with Δ[Hb].

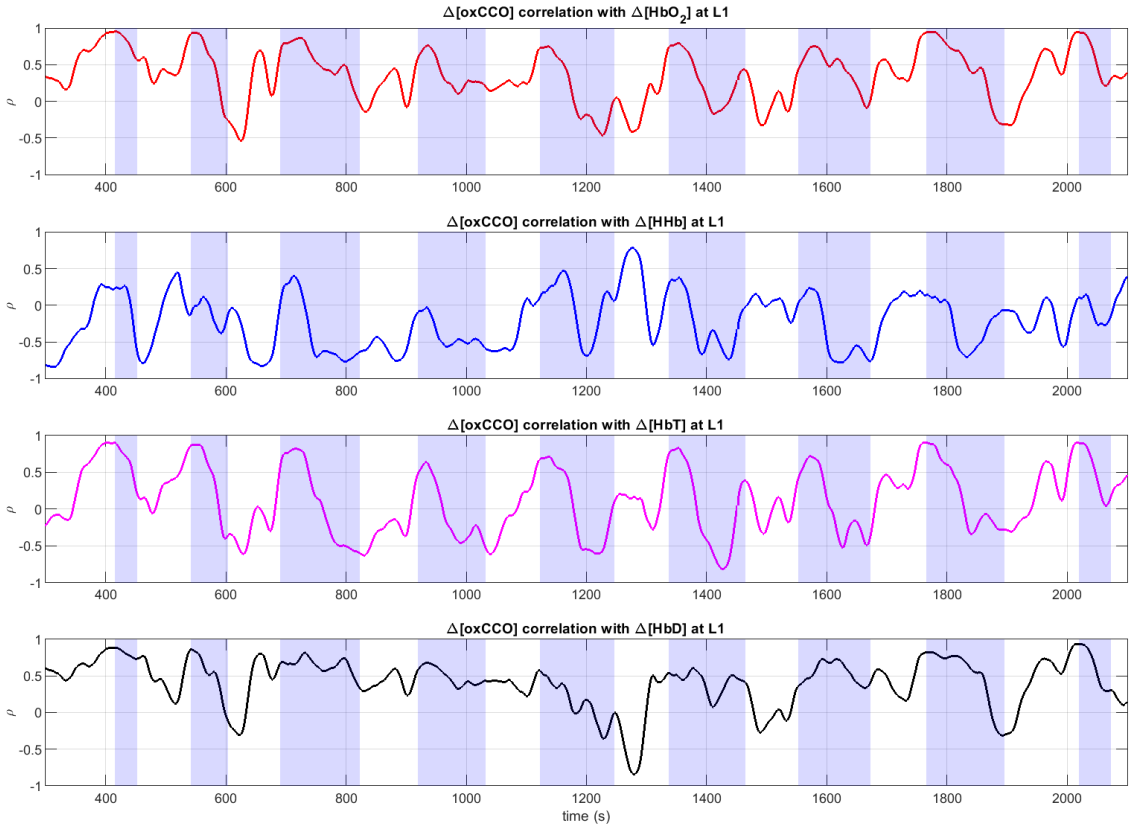

(a) L1

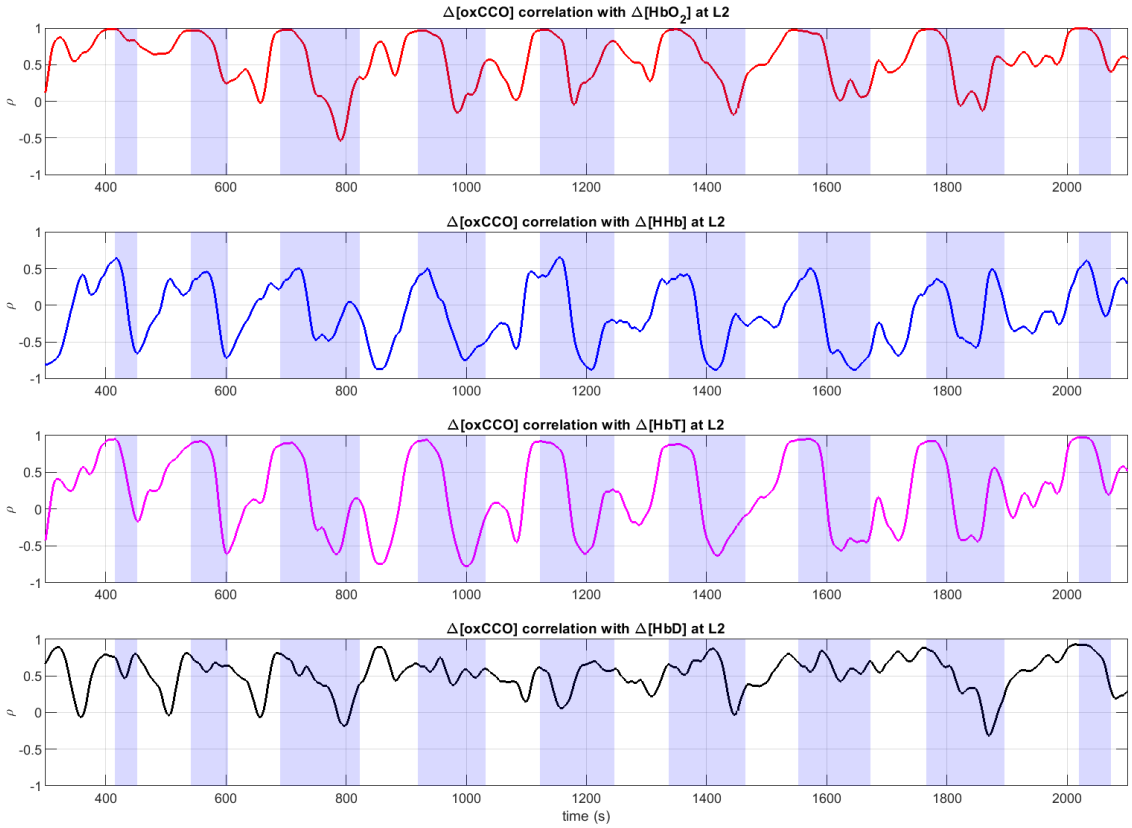

(b) L2

Figure 42: Δ[oxCCO] correlation with Δ[Hb].

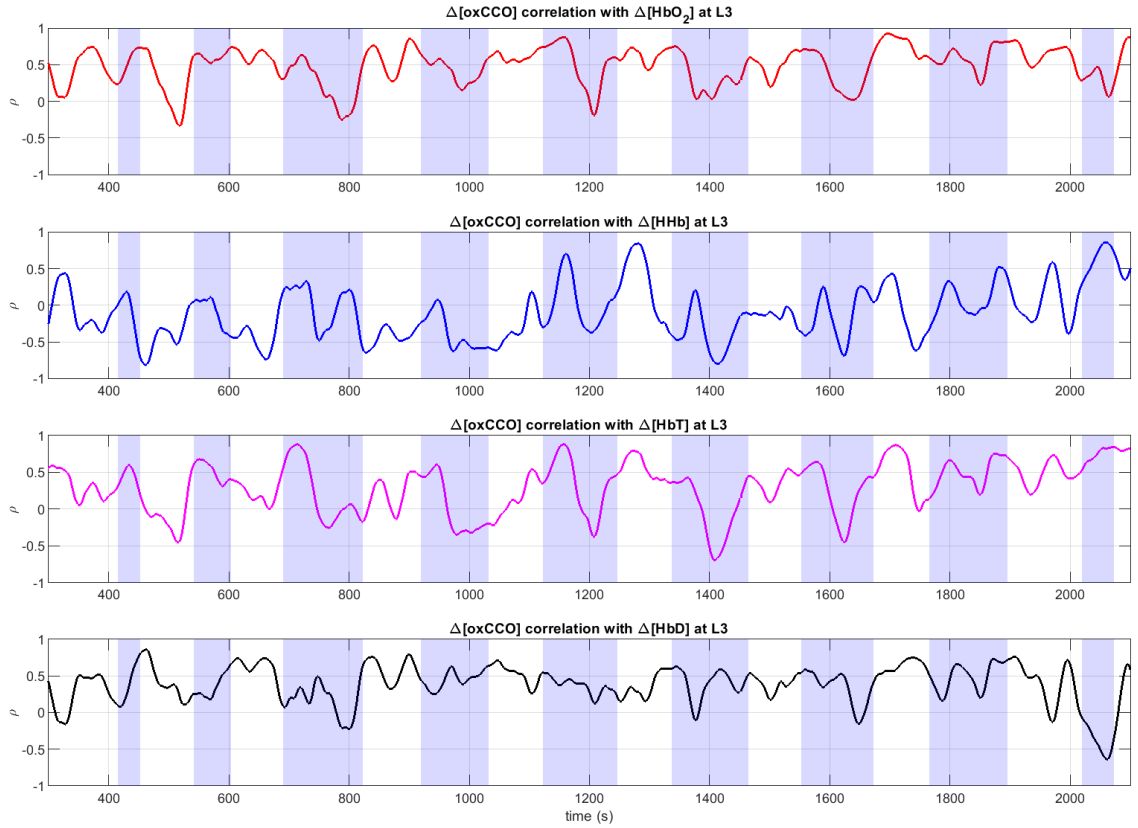

(a) L3

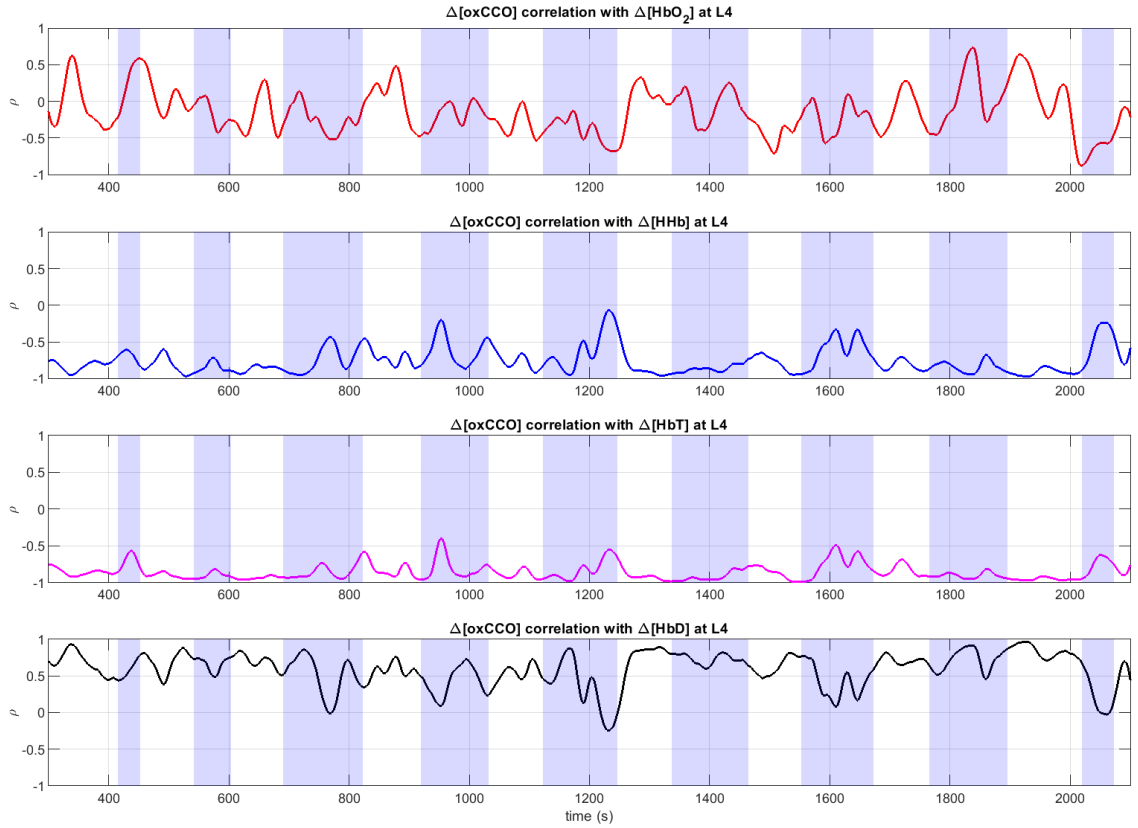

(b) L4

Figure 43: Δ[oxCCO] correlation with Δ[Hb].

4.7 PCA and clustering of waveforms after seizure detection times

The haemodynamic response (HR) seen in EEG–fNIRS studies on ictal data [16, 29, 45] is also seen in this data. Each cluster's waveform is the mean waveforms for that cluster. First the dimensions of 136 waveforms were reduced by PCA, then clustered into k clusters by k-means. The increase of $\Delta[HbO_2]$ is the most striking feature and is consistent with most studies of newborns [12].

Although k=8, k=4, and k=2 were tried, only the results from k=2 are in the figures below. This choice was based on domain expertise.

4.7.1 NIRS $\Delta[HbO_2]$ waveforms

Figure 44 shows the mean $\Delta[HbO_2]$ waveforms for two k-means clusters.

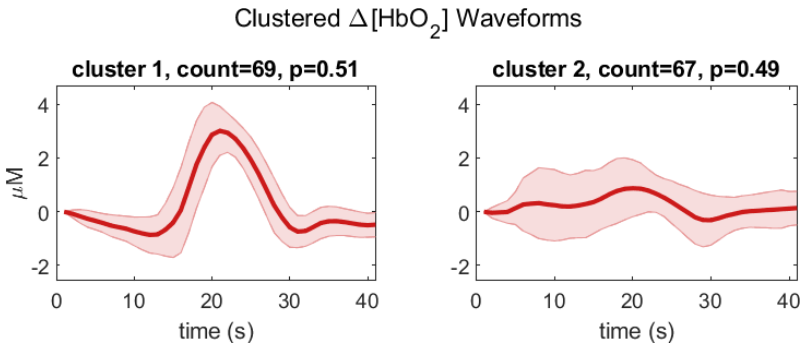

(a)

(b)

Figure 44: K-means clustered waveforms, 40s after detection, k=2.

4.7.2 NIRS Δ[HHb] waveforms

Figure 45 shows the Δ[HHb] waveforms in two clusters. Cluster 1 waveforms dominate R5, R1, L3, and R3.

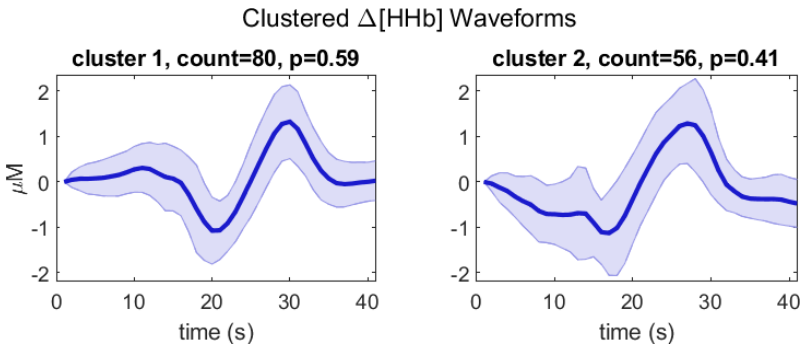

(a)

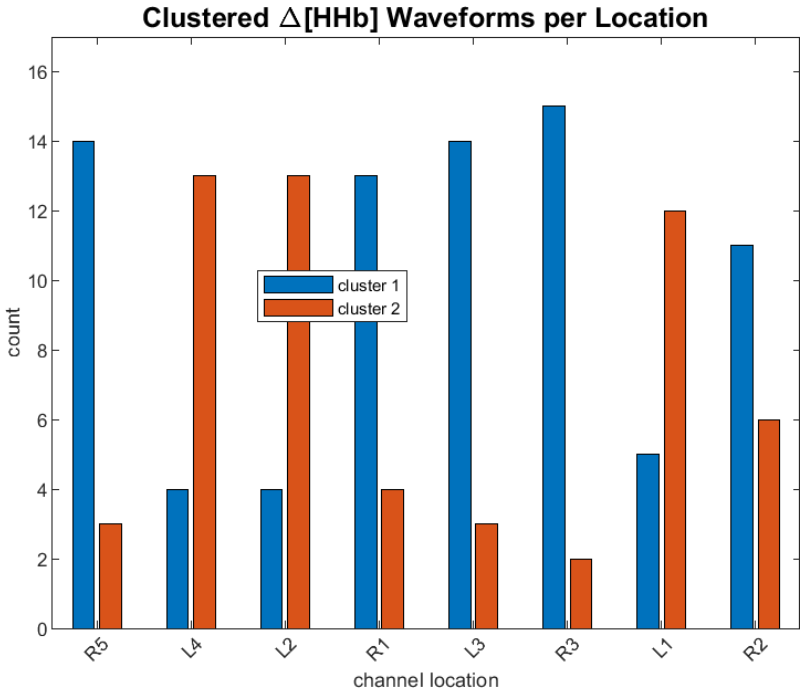

(b)

Figure 45: K-means clustered waveforms, 40s after detection, k=2.

4.7.3 NIRS Δ[oxCCO] waveforms

In Figure 46(a) the 136 waveforms are clustered into two groups, which may be classified as flat and negative responses.

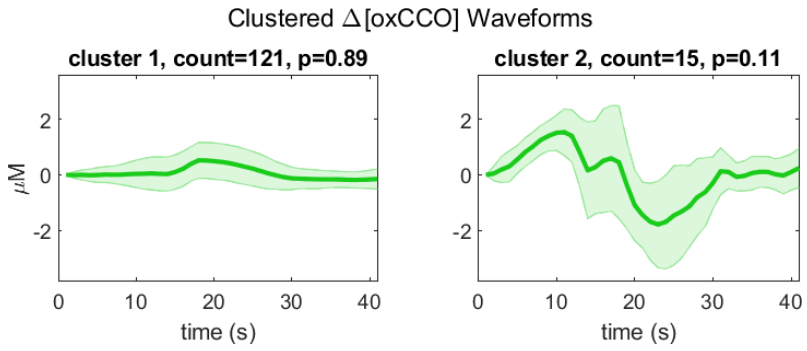

(a)

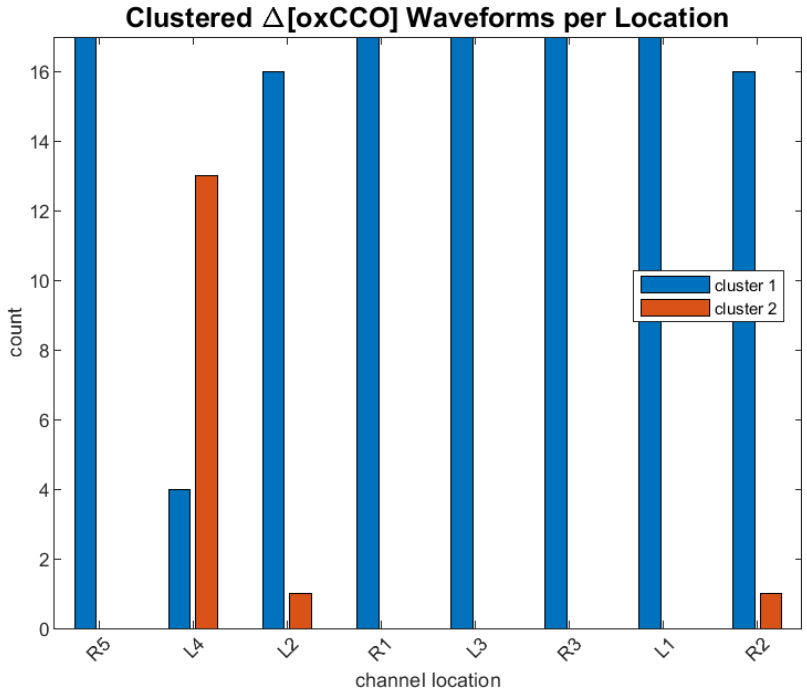

(b)

Figure 46: K-means clustered waveforms, 40s after detection, k=2: (a) waveforms, (b) waveform counts at each channel location.

5 Discussion

5.1 FFTs and spectrograms

The FFT for EEG location F3 had the highest intensity for frequencies below 5Hz, Figure 15. This is consistent with Figure 16 where the power/frequency (dB/Hz) is noticeably greater at F3 than at other locations. EEG F3 is close to NIRS channel L2, so L2 should be under more stress than other areas.

The spectrograms for NIRS $\Delta[HbO_2]$ are shown in Figures 18 and 19. The seizures are distinct at L1, L2, and R3 (the bright yellow patches can be easily counted). The spectrograms for Δ[oxCCO] are shown in Figures 20 and 21. Seizures are distinct at L1 and L2.

While EEG is the gold standard, the seizures are more visible in the NIRS $\Delta[HbO_2]$ spectrograms, and the Δ[oxCCO] spectrograms indicate greater metabolic demands at L1 and L2. In any event, the spectrograms confirm that NIRS can

detect seizures, and even the metabolic response by Δ[oxCCO].

5.2 Mean EEG waveforms

Figures 23 and 25 show, for example, that unfiltered and filtered EEG F3 traces can be highly correlated with filtered NIRS Δ[HbO_2] at L2. However, the combination and order in which `decimate`, `abs`, `smooth`, and `trapz` are invoked can have a large impact the computed value of ρ, as can choice of filter, window size, phase shift, jitter, and various parameters.

5.3 Mean NIRS waveforms

5.3.1 Some individual NIRS waveforms are similar to the classic HRF

The shape of the haemodynamic response function (HRF) for adults is well known, as in Figure 47, but not for developmental populations [12]. Some results suggest that the infant HRF is delayed, slower to peak and/or return to baseline than in adults [27].

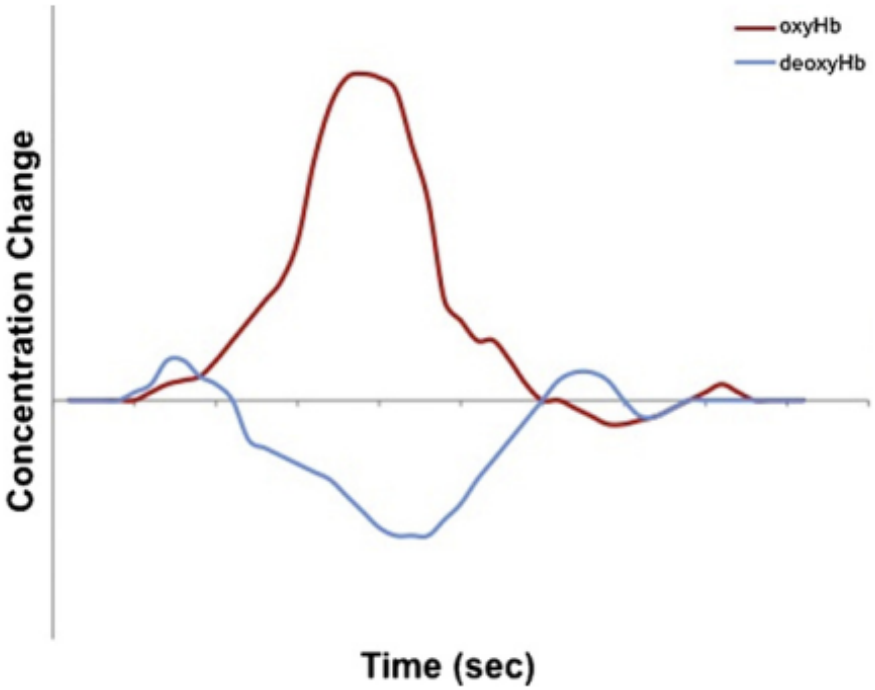

Figure 47: The typical HRF in adults peaks several seconds after stimulus. Image: [17].

Figure 48 shows a clip of filtered NIRS data recorded from location L2. Although on different scales, the haemodynamic and metabolic responses are synchronised with seizure onsets (start of shaded areas). On average, the Δ[HbO_2] waveform at L2 peaks about 21s after seizure onset, time from initial dip to peak to second dip are ∼9s each. This suggests a tight coupling between the oxygen delivery and oxygen utilization at this location (in this patient). This is significant because in cases where brain injury resulted in an unfavourable outcome, the mitochondrial function was more dependent on oxygenation [3]. Possibly due to lack of buffering capacity. So, the correlation of Δ[oxCCO] with Δ[HbT] and Δ[HbD] is also significant.

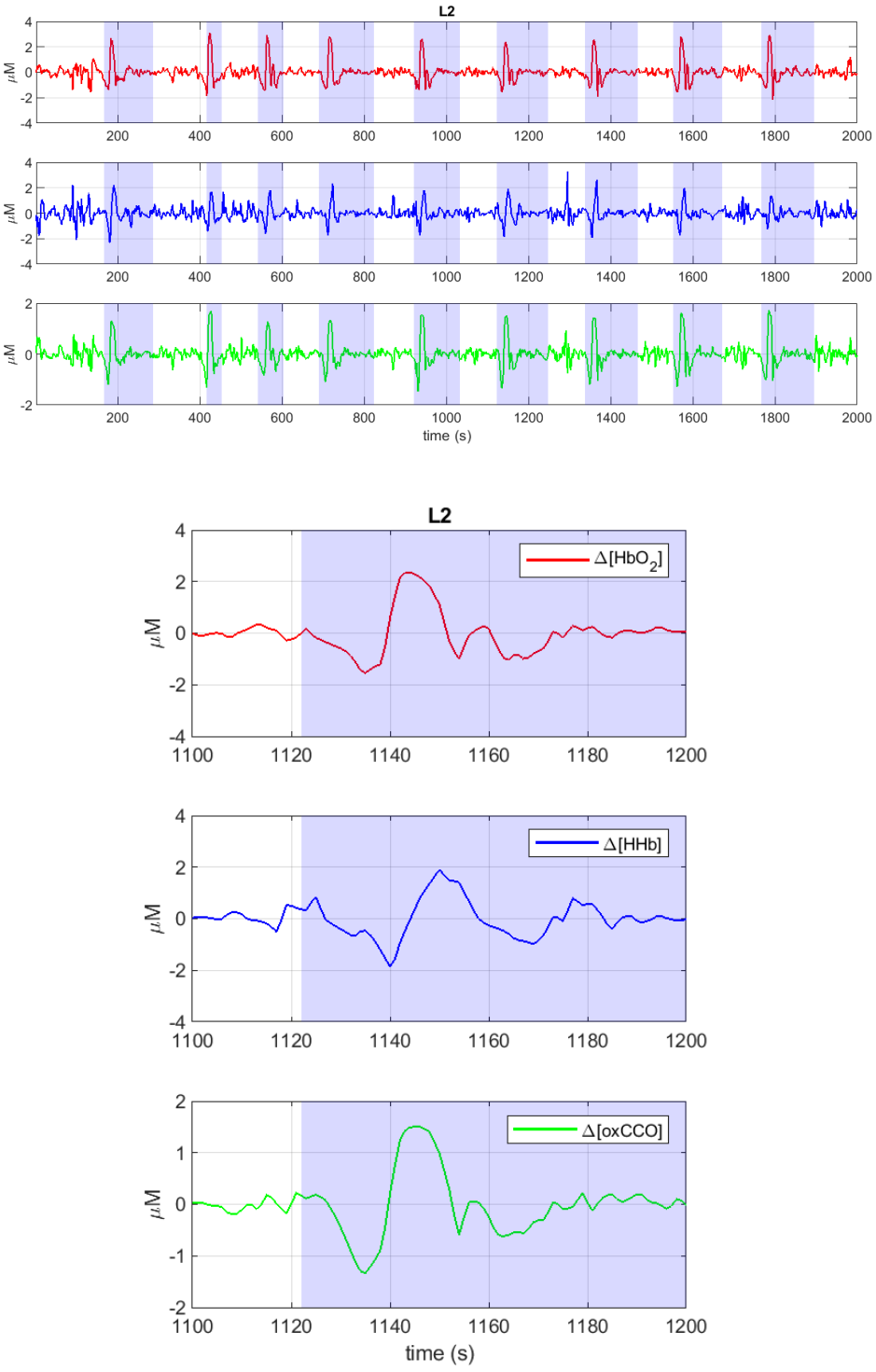

Figure 48: Filtered NIRS data: $\Delta[HbO_2]$, $\Delta[HHb]$, and $\Delta[oxCCO]$ from L2. **Top**: Seizures are indicated by the shaded areas. The y axis scales are different, but the timing and shape of the response is similar. **Bottom**: synchronised waveforms, note the large $\Delta[oxCCO]$ initial dip.

5.3.2 Peak aligned NIRS waveforms

According to this patient's history, seizures start in the left posterior region. They present with fast rhythmic activity which usually evolves into generalised spikewave discharges in a few seconds. NIRS channels L3 and L4 are closest to the posterior

area, so the seizures could to spread to them before L1 and L2.

The statistics for the peak aligned waveforms in Table 1 shows that HR at L3 and L4 peaks sooner than at L1 and L2. The 40 second window must be shifted left by -3 and -4 seconds for L3 and L4, and only -2 and -2 for L1 and L2. On average seizures reach L3 and L4 ∼1.5s before they reach L1 and L2, consistent with the detection time waveforms in Figures 30 to 33.

5.3.3 Detection aligned NIRS waveforms

In Figures 30, 31, 32, 33 each waveform is the mean of 17 seizures during 40s after detection time. Onset times are known, so averaging data points is an appropriate data driven method [33].

For this patient, waveform shape varies substantially between NIRS channel locations. The $\Delta[HbO_2]$ waveform is relatively consistent and usually peaks ∼20s after the seizure detection. Most of these waveforms show a typical HRF shape including an initial dip before ascending to the peak, and a dip below the baseline when returning to baseline. The positive increase agrees with the majority of results reviewed by [12].

The mean Δ[HHb] waveforms for this patient are not mixed, as expected [12]. An initial increase is not apparent, but they consistently show a typical HR shape that decreases to a minimum at ∼20s followed by an overshoot that peaks at ∼90s when returning to baseline.

While Δ[oxCCO] increases to a peak at ∼20s, Δ[HHb] decreases to a nadir at ∼20s and, consequently, Δ[HbD] increases to its peak at the same time. This is consistent with the HR that NIRS is expected to measure.

Most of the mean Δ[oxCCO] waveforms are flat. The positive responses at R1 and R2 are very small. But the response of Δ[oxCCO] at L4 is an increase followed by a decrease that is negatively correlated with the Δ[HHb] waveform. L2 is the only location that has a smooth positive response that is tightly coupled with the HR.

5.4 Correlation of EEG with each NIRS channel depends on location

The correlation of EEG with the NIRS channels depends on EEG location. For example:

- Figure 34(a,b): EEG F3 correlation with Δ[oxCCO] goes from the most positive to the most negative.
- Figure 35(b): EEG F4 correlation with $\Delta[HbO_2]$ is the most positive, increases after detection.
- Figure 36(a,b): EEG C3 correlation with Δ[HHb] is the most negative after detection.
- Figure 37(a,b): EEG C4 correlation with $\Delta[HbO_2]$ is the most positive, increases after detection.

Correlation also depends on one detection time per seizure; some locations will be out of phase.

5.5 Correlation of EEG with proximate NIRS channels

If EEG and NIRS are working correctly, then recordings from proximate locations should be more correlated that recordings from distant locations. Figure 38 showed the correlation of each EEG with proximate NIRS channels 40s before and after seizure detection.

The correlation of EEG traces paired with proximate NIRS channels is higher than with all NIRS channels, as reported in Section 4.6.3, This was supported by the data in Table 2 where the mean was based on all correlations (regardless of each statistical significance). For example, after detection paired $\Delta[HbO_2]$ ρ was 0.327, greater than unpaired ρ of 0.308, and after detection paired Δ[HHb] ρ was -0.214, greater than unpaired ρ of -0.197. Δ[CCO] was the only exception. And the same pattern holds true for paired versus unpaired correlation before seizure detection.

	HbO2	HHb	HbT	HbD	CCO
Paired before	0.260	-0.114	0.168	0.281	0.267
Paired after	**0.327**	**-0.214**	**0.117**	**0.306**	**-0.031**
Unpaired before	0.216	-0.101	0.140	0.241	0.318
Unpaired after	**0.308**	**-0.197**	**0.072**	**0.277**	**-0.087**

Table 2: Mean correlation ρ of unpaired EEG with NIRS during the 40s before versus during the 40s after detection. Note: these are means of correlations regardless of statistical significance.

Correlations ρ with p-values ≥ 0.5 are shown as zero in the figures, but the original values were used to calculate the means in Table 2.

However, the correlation of EEG with NIRS also depends on detection time, window size, and filtering. For example, applying a 15 to 25Hz bandpass filter to the EEG leads to different results and, hopefully, an answer to a different question.

5.6 Correlation of Δ[oxCCO] with the Δ[Hb] at each NIRS channel

In Figure 39, Δ[oxCCO] is highly correlated with $\Delta[HbO_2]$ before detection, but the correlation is negative at L4 and R2. After detection there is no correlation at R2. Δ[oxCCO] is more negatively correlated with Δ[HHb] after detection. Δ[oxCCO] is more positively correlated with Δ[HbD] after detection. In general, this consistent with the mean waveforms presented in this report.

5.7 Correlation of Δ[oxCCO] with Δ[Hb] during a sliding time window may be predict seizures

In Figure 40(b), at R2 Δ[oxCCO] correlation with $\Delta[HbO_2]$ increases greatly until it reaches a peak at the time of seizure onset. Δ[oxCCO] correlation with Δ[HbD] shows the same pattern. And the same pattern appears at R5, L1, and L2, Figures 41(b) and 42. Strong relationships between cerebral metabolism and metabolic metabolism with neuronal activation and energy demand seen in the data indicate a poor prognosis [3].

Δ[HbT] also clearly peaks at time of seizure onset at R5, L1 and L2. Correlation at other locations is not tightly coupled with the HRF, but some spatial variability is expected.

5.8 PCA and clustering of NIRS waveforms after seizure detection

An increase of $\Delta[HbO_2]$ has been reported by most studies of newborns [12]. Positive $\Delta[HbO_2]$ waveforms are typical in this data set is their, they tend to peak about $\sim$20s after seizure onset.

Figure 44 showed two clusters: the strong HR's are in cluster 1 and the weak in cluster 2 in almost equal proportions. Figure 44(b): strong HR waveforms were mostly recorded from R5, L2, R3, L1. Locations L4, L3, and R2 were dominated by weak HRs.

Figure 45 shows the Δ[HHb] waveforms in two clusters. Cluster 1 waveforms dominate R5, R1, L3, and R3. This waveform is interesting because it shows an initial increase.

When the Δ[oxCCO] data was clustered into 4 waveforms, a very flat response cluster dominated with 106 members. After clustering into two clusters, 121/136 waveforms were associated with cluster 1, the slightly positive waveform. The cluster 2 waveform shows an increase followed by a decrease, most were recorded from L4. A sudden increase in Δ[oxCCO] is consistent mat be expected at the start of a seizure [28]. The decrease in [oxCCO] indicates hypoxia [39].

While the focus of this report has been on seizures, it should be kept in mind that neuronal activity is not always the stimulus for the haemodynamic and metabolic response. Many different stimuli can produce correlations between the haemoglobins and the cytochrome; stimuli such as hyperoxia, hypoxia, hypercapnia, and so on, not just seizures [Dr Ilias Tachtsidis, UCL]. Pre-ictal signals may be elicited by astrocyte or pericyte mediated signaling or local potassium and local neurotransmitter/neuropeptide release [14, 18, 32, 43]. Haemodynamic changes may be influenced by glia (such as astrocytes), which are not directly recorded with standard electrophysiological methods [31].

6 Future Work

Test the hypotheses generated by this report. This could involve more frequency and phase analysis. For example, although the EEG correlates with the NIRS data, is the correlation greater for some frequency bands than other? Does the haemodynamic and/or the metabolic response resonate differently with some frequency bands? Or, is the sum of neuronal activity over some time period time the most important factor? Phase shifting can increase correlation, but what is the question?

A rigorous statistical analysis could be applied to some of the results. It is easy to present p-values, but they can be misleading. There are many ways to visualise this data set and many way to compute various correlations and so on, some are in this report, but many more were excluded for brevity. Many variations of the methods presented are plausible. So there are many chances to discover the p-values you want that are not valid [19].

After valid statistical results have been found, those results may be linked to the physiology. Which brain areas have the best or worst physiology? Which brain areas are most likely suffer damage in the future? In other words, can the NIRS data really provide useful information about seizure prediction, detection, monitoring, diagnosis and prognosis?

7 Conclusion

The preliminary results reported in this paper support the view that NIRS data can be used for seizure detection and monitoring conditions before and after seizures. The NIRS data generally agrees with the EEG data; the mean EEG traces near the time of seizure detection show features that align very well with features, especially the peak times, of the $\Delta[HbO_2]$ waveforms recorded from proximate NIRS channels. This was also evident in the spectrograms.

Analysis of the NIRS data showed that the HR depends on local physiological conditions, and the peak aligned waveforms suggested that the NIRS data can confirm the temporal and spatial order in which each seizure spreads.

Prediction is less clear, but the positive correlation of Δ[oxCCO] with both $\Delta[HbO_2]$ and the oxygenation difference, $\Delta[HbO_2] - \Delta[HHb]$, tend to increase to a peak before seizure onset. Data from patients with highly variable intervals between seizures is needed to better assess the utility of NIRS for seizure prediction.

References

[1] Dizem Arifler, Tingting Zhu, Sara Madaan, and Ilias Tachtsidis. Optimal wavelength combinations for near-infrared spectroscopic monitoring of changes in brain tissue hemoglobin and cytochrome c oxidase concentrations. *Biomedical optics express*, 6:933–947, March 2015.

[2] Gemma Bale, Clare E Elwell, and Ilias Tachtsidis. From jöbsis to the present day: a review of clinical near-infrared spectroscopy measurements of cerebral cytochrome-c-oxidase. *Journal of biomedical optics*, 21:091307, September 2016.

[3] Gemma Bale, Subhabrata Mitra, Isabel de Roever, Magdalena Sokolska, David Price, Alan Bainbridge, Roxana Gunny, Cristina Uria-Avellanal, Giles S Kendall, Judith Meek, et al. Oxygen dependency of mitochondrial metabolism indicates outcome of newborn brain injury. *Journal of Cerebral Blood Flow & Metabolism*, page 0271678X18777928, 2018.

[4] Gemma Bale, Subhabrata Mitra, Judith Meek, Nicola Robertson, and Ilias Tachtsidis. A new broadband near-infrared spectroscopy system for in-vivo measurements of cerebral cytochrome-c-oxidase changes in neonatal brain injury. *Biomedical optics express*, 5:3450–3466, October 2014.

[5] Samuel F Berkovic, John C Mulley, Ingrid E Scheffer, and Steven Petrou. Human epilepsies: interaction of genetic and acquired factors. *Trends in neurosciences*, 29:391–397, July 2006.

[6] G M Boynton, S A Engel, G H Glover, and D J Heeger. Linear systems analysis of functional magnetic resonance imaging in human v1. *The Journal of neuroscience : the official journal of the Society for Neuroscience*, 16:4207–4221, July 1996.

[7] Ivan Cohen, Vincent Navarro, Stéphane Clemenceau, Michel Baulac, and Richard Miles. On the origin of interictal activity in human temporal lobe epilepsy in vitro. *Science (New York, N.Y.)*, 298:1418–1421, November 2002.

[8] Michael X Cohen. Where does eeg come from and what does it mean? *Trends in neurosciences*, 40:208–218, April 2017.

[9] Robert Cooper, Juliette Selb, Louis Gagnon, Dorte Phillip, Henrik W Schytz, Helle K Iversen, Messoud Ashina, and David A Boas. A systematic comparison of motion artifact correction techniques for functional near-infrared spectroscopy. *Frontiers in neuroscience*, 6:147, 2012.

[10] Rosa Cossart, Christophe Bernard, and Yehezkel Ben-Ari. Multiple facets of gabaergic neurons and synapses: multiple fates of gaba signalling in epilepsies. *Trends in neurosciences*, 28:108–115, February 2005.

[11] Isabel de Roever, Gemma Bale, Robert J Cooper, and Ilias Tachtsidis. Functional nirs measurement of cytochrome-c-oxidase demonstrates a more brain-specific marker of frontal lobe activation compared to the haemoglobins. In *Oxygen Transport to Tissue XXXIX*, pages 141–147. Springer, 2017.

[12] Isabel de Roever, Gemma Bale, Subhabrata Mitra, Judith Meek, Nicola J Robertson, and Ilias Tachtsidis. Investigation of the pattern of the hemodynamic response as measured by functional near-infrared spectroscopy (fnirs) studies in newborns, less than a month old: A systematic review. *Frontiers in human neuroscience*, 12:371, 2018.

[13] Alexander S Ecker, Philipp Berens, Georgios A Keliris, Matthias Bethge, Nikos K Logothetis, and Andreas S Tolias. Decorrelated neuronal firing in cortical microcircuits. *Science (New York, N.Y.)*, 327:584–587, January 2010.

[14] Jessica A Filosa, Adrian D Bonev, Stephen V Straub, Andrea L Meredith, M Keith Wilkerson, Richard W Aldrich, and Mark T Nelson. Local potassium signaling couples neuronal activity to vasodilation in the brain. *Nature neuroscience*, 9:1397–1403, November 2006.

[15] Maria Angela Franceschini, Sergio Fantini, John H Thompson, Joseph P Culver, and David A Boas. Hemodynamic evoked response of the sensorimotor cortex measured noninvasively with near-infrared optical imaging. *Psychophysiology*, 40(4):548–560, 2003.

[16] Anne Gallagher, Maryse Lassonde, Danielle Bastien, Phetsamone Vannasing, Frédéric Lesage, Christophe Grova, Alain Bouthillier, Lionel Carmant, Franco Lepore, Renée Béland, and Dang Khoa Nguyen. Non-invasive pre-surgical investigation of a 10 year-old epileptic boy using simultaneous eeg-nirs. *Seizure*, 17:576–582, September 2008.

[17] Judit Gervain, Jacques Mehler, Janet F Werker, Charles A Nelson, Gergely Csibra, Sarah Lloyd-Fox, Mohinish Shukla, and Richard N Aslin. Near-infrared spectroscopy: a report from the mcdonnell infant methodology consortium. *Developmental cognitive neuroscience*, 1(1):22–46, 2011.

[18] Edith Hamel. Perivascular nerves and the regulation of cerebrovascular tone. *Journal of applied physiology (Bethesda, Md. : 1985)*, 100:1059–1064, March 2006.

[19] John P A Ioannidis. Why most published research findings are false. *PLoS medicine*, 2:e124, August 2005.

[20] Anil K Jain. Data clustering: 50 years beyond k-means. *Pattern recognition letters*, 31(8):651–666, 2010.

[21] Anil K Jain, M Narasimha Murty, and Patrick J Flynn. Data clustering: a review. *ACM computing surveys (CSUR)*, 31(3):264–323, 1999.

[22] Anna-Maria Katsarou, Aristea S Galanopoulou, and Solomon L Moshé. Epileptogenesis in neonatal brain. *Seminars in fetal & neonatal medicine*, 23:159–167, June 2018.

[23] Christina Kolyva, Arnab Ghosh, Ilias Tachtsidis, David Highton, Chris E Cooper, Martin Smith, and Clare E Elwell. Cytochrome c oxidase response to changes in cerebral oxygen delivery in the adult brain shows higher brain-specificity than haemoglobin. *Neuroimage*, 85:234–244, 2014.

[24] Michael S Lewicki. A review of methods for spike sorting: the detection and classification of neural action potentials. *Network: Computation in Neural Systems*, 9(4):R53–R78, 1998.

[25] James MacQueen et al. Some methods for classification and analysis of multivariate observations. In *Proceedings of the fifth Berkeley symposium on mathematical statistics and probability*, volume 1, pages 281–297. Oakland, CA, USA, 1967.

[26] S J Matcher, C E Elwell, C E Cooper, M Cope, and D T Delpy. Performance comparison of several published tissue near-infrared spectroscopy algorithms. *Analytical biochemistry*, 227:54–68, May 1995.

[27] Judith Meek. Basic principles of optical imaging and application to the study of infant development. *Developmental Science*, 5(3):371–380, 2002.

[28] Subhabrata Mitra, Gemma Bale, Sean Mathieson, Cristina Uria-Avellanal, Judith Meek, Ilias Tachtsidis, and Nicola J Robertson. Changes in cerebral oxidative metabolism during neonatal seizures following hypoxic-ischemic brain injury. *Frontiers in pediatrics*, 4:83, 2016.

[29] Dang Khoa Nguyen, Julie Tremblay, Philippe Pouliot, Phetsamone Vannasing, Olivia Florea, Lionel Carmant, Franco Lepore, Mohamad Sawan, Frédéric Lesage, and Maryse Lassonde. Non-invasive continuous eeg-fnirs recording of temporal lobe seizures. *Epilepsy research*, 99:112–126, March 2012.

[30] E Niedermeyer and F H Lopes da Silva. *Electroencephalography: Basic Principles, Clinical Applications and Related Fields*. Lippincott Williams and Wilkins, 2005.

[31] Kunal S Patel, Mingrui Zhao, Hongtao Ma, and Theodore H Schwartz. Imaging preictal hemodynamic changes in neocortical epilepsy. *Neurosurgical focus*, 34:E10, April 2013.

[32] Claire M Peppiatt, Clare Howarth, Peter Mobbs, and David Attwell. Bidirectional control of cns capillary diameter by pericytes. *Nature*, 443:700–704, October 2006.

[33] Paola Pinti, Arcangelo Merla, Clarisse Aichelburg, Frida Lind, Sarah Power, Elizabeth Swingler, Antonia Hamilton, Sam Gilbert, Paul W Burgess, and Ilias Tachtsidis. A novel glm-based method for the automatic identification of functional events (aide) in fnirs data recorded in naturalistic environments. *NeuroImage*, 155:291–304, July 2017.

[34] R Quian Quiroga, Zoltan Nadasdy, and Yoram Ben-Shaul. Unsupervised spike detection and sorting with wavelets and superparamagnetic clustering. *Neural computation*, 16(8):1661–1687, 2004.

[35] Hernan Gonzalo Rey, Carlos Pedreira, and Rodrigo Quian Quiroga. Past, present and future of spike sorting techniques. *Brain research bulletin*, 119:106–117, 2015.

[36] Felix Scholkmann, Stefan Kleiser, Andreas Jaakko Metz, Raphael Zimmermann, Juan Mata Pavia, Ursula Wolf, and Martin Wolf. A review on continuous wave functional near-infrared spectroscopy and imaging instrumentation and methodology. *Neuroimage*, 85:6–27, 2014.

[37] Gary Strangman, Joseph P Culver, John H Thompson, and David A Boas. A quantitative comparison of simultaneous bold fmri and nirs recordings during functional brain activation. *NeuroImage*, 17:719–731, October 2002.

[38] Abdulhamit Subasi and M Ismail Gursoy. Eeg signal classification using pca, ica, lda and support vector machines. *Expert systems with applications*, 37(12):8659–8666, 2010.

[39] Martin M Tisdall, Ilias Tachtsidis, Terence S Leung, Clare E Elwell, and Martin Smith. Near-infrared spectroscopic quantification of changes in the concentration of oxidized cytochrome c oxidase in the healthy human brain during hypoxemia. *Journal of biomedical optics*, 12:024002, 2007.

[40] Martin M Tisdall, Ilias Tachtsidis, Terence S Leung, Clare E Elwell, and Martin Smith. Changes in the attenuation of near infrared spectra by the healthy adult brain during hypoxaemia cannot be accounted for solely by changes in the concentrations of oxy- and deoxy-haemoglobin. *Advances in experimental medicine and biology*, 614:217–225, 2008.

[41] Mona C Toet and Petra M A Lemmers. Brain monitoring in neonates. *Early human development*, 85:77–84, February 2009.

[42] F Wallois, A Patil, C Héberlé, and R Grebe. Eeg-nirs in epilepsy in children and neonates. *Neurophysiologie clinique = Clinical neurophysiology*, 40:281–292, 2010.

[43] Xiaohai Wang, Nanhong Lou, Qiwu Xu, Guo-Feng Tian, Wei Guo Peng, Xiaoning Han, Jian Kang, Takahiro Takano, and Maiken Nedergaard. Astrocytic ca2+ signaling evoked by sensory stimulation in vivo. *Nature neuroscience*, 9:816–823, June 2006.

[44] Martin Wolf, Ursula Wolf, Vlad Toronov, Antonios Michalos, L Adelina Paunescu, Jee Hyun Choi, and Enrico Gratton. Different time evolution of oxyhemoglobin and deoxyhemoglobin concentration changes in the visual and motor cortices during functional stimulation: a near-infrared spectroscopy study. *Neuroimage*, 16(3):704–712, 2002.

[45] Meryem A Yücel, Juliette Selb, David A Boas, Sydney S Cash, and Robert J Cooper. Reducing motion artifacts for long-term clinical nirs monitoring using collodion-fixed prism-based optical fibers. *NeuroImage*, 85 Pt 1:192–201, January 2014.